A homogenization model for porous ductile solids under cyclic loads comprising a matrix with isotropic and linear kinematic hardening

Long Cheng, Kostas Danas, Andrei Constantinescu, Djimedo Kondo

A homogenization model for porous ductile solids under cyclic loads comprising a matrix with isotropic and linear kinematic hardening

L. Cheng[a,*], K. Danas[a], A. Constantinescu[a], D. Kondo[b]

[a] *Laboratoire de Mécanique des Solides, École Polytechnique, Université Paris-Saclay, Palaiseau, France*
[b] *Institut Jean Le Rond d'Alembert, UMR 7190 CNRS, Université Pierre et Marie Curie, 4 place Jussieu, F75005 Paris, France*

Abstract

In this work, we propose an semi-analytical micromechanical model to study the elasto-plastic response of porous materials subjected to cyclic loading with isotropic and linear kinematic hardening at finite strains. To this end, we use an approximate but numerically efficient decoupled homogenization strategy between the elastic and plastic parts. The resulting effective back stress in the porous solid, similar to the macroscopic stress and plastic strain, has non-zero hydrostatic terms and depends on the porosity, the void shape and orientation as a result of the homogenization process. Subsequently, a complete set of equations is defined to describe the evolution of the microstructure, i.e., void volume fraction (porosity), (ellipsoidal) void shape and orientation both in the elastic and the plastic regimes. The model is then numerically implemented in a general purpose user-material subroutine. Full field finite element simulations of multi-void periodic unit cells are used to assess the predictions of the proposed model. The latter is found to be in good qualitative and quantitative agreement with the finite element results for most of the loading types, hardening parameters and porosities considered in this study, but is less accurate for very small porosities. The combined analytical and numerical study shows that elasticity is an important mechanism for porosity ratcheting in addition to strain hardening. Specifically, in order to recover the main qualitative features of porosity ratcheting for all cyclic loads considered in the present study, it is shown to be critical to take into account the evolution of the microstructure not only during the plastic loading, as is the usual hypothesis, but also during elastic loading. Finally, the effect of isotropic and linear kinematic hardening is found to be highly non-monotonic and non-trivial upon porosity ratcheting for most cases considered here.

Keywords: Cyclic loading, Porous ductile material, Porosity ratcheting, Non-linear homogenization, Strain hardening, Elasto-plasticity

*Corresponding author.
Email addresses: cheng@lms.polytechnique.fr (L. Cheng), kdanas@lms.polytechnique.fr (K. Danas)

1. Introduction

A large number of studies has been devoted the last years to the modeling of elasto-plastic porous materials. Most of those studies focused on monotonic loading conditions, isotropic hardening of the matrix and subsequent ductile damage prediction. The number of works on this topic are numerous and will not be referred to here. On the other hand very few studies up to date have dealt with the cyclic response of such porous solids. Several of the questions that arise when cyclic loading is applied are related to elasticity effects, the presence of kinematic hardening, the use of small or finite strains to analyze the problem, the amplitude of the overall stress/strain that is applied, the stress triaxiality and Lode parameter or even anisotropy effects introduced by the void shape and orientation, void shape and orientation effects and ultimately the number of cycles analyzed. Obviously all these questions cannot be addressed in a single paper but are important to the study of cyclic loading and fatigue of such materials.

Advances in imaging techniques (SEM and tomography) have clearly revealed the presence of voids in metals. Recently, Limodin et al. (2014), Dezecot et al. (2016) and Dahdah et al. (2016) have obtained 3D tomographic images for aluminum alloys manufactured by lost-foam-casting fabrication techniques. Voids of various sizes and shapes (spherical, ellipsoidal but also non-canonical) were observed. The presence of initial voids as well as of secondary porosity resulting from debonding and/or fracturing of second phase particles was found to be critical for the fatigue life of such solids. The significance of voids has also been studied in a different context by Charkaluk et al. (2014), where a probability density function using a quantitative analysis of the microstructure of the material was used to characterize the fatigue lifetime.

From the micromechanical point of view, early studies by Devaux et al. (1997); Brocks and Steglich (2003); Besson and Guillemer-Neel (2003); Rabold and Kuna (2005) and Kondo et al. (2003) have explored numerically and analytically the cyclic response of porous materials at small and moderate number of cycles with a main emphasis on axisymmetric loading states at large strains. Their analysis has mainly focused on the prediction of porosity ratcheting, which is a critical mechanism for fatigue fracture. In particular, in Devaux et al. (1997), porosity ratcheting has been attributed to asymmetries between tension and compression mainly due to hardening and elasticity. Besson and Guillemer-Neel (2003) has proposed a rather complete model that takes into account isotropic and nonlinear kinematic hardening in the matrix combined into a modified Gurson (1977) model. While his study has revealed a striking effect of void growth and ratcheting when that model was used in structural calculations, it was stated that the model itself predicts poorly the ratcheting effect. Subsequent studies by Pirondi et al. (2006) and Hommel and Meschke (2010) have attempted to further calibrate those models for porous materials in order to analyze experimental axisymmetric specimens. This proved a difficult task and use of a large number of additional parameters was required. Yield surface evolution of the cyclically loaded porous material has been studied by Seifert and Schmidt (2009). Yet, those models have proven insufficient to describe the low-cycle response of the experimental specimens, especially at lower triaxialities. Moreover, micromechanical models of porous material with ellipsoidal

voids have been proposed in literature particularly in the case of monotonic loading (see for example Gologanu and Leblond (1993); Leblond and Gologanu (2008)). Two more recent studies, the first purely numerical (Mbiakop et al., 2015a) and the second numerical and analytical Lacroix et al. (2016) have contributed further to the understanding of the macroscopic response of porous materials under cyclic loading.

Specifically, Mbiakop et al. (2015a) has carried out an extensive parametric study to investigate the effects of stress triaxiality, Lode angle, initial void shapes, matrix elasticity and isotropic (but much less kinematic) hardening upon the cyclic response of periodic porous solids. Following, similar observations by Devaux et al. (1997) (see also Mbiakop et al. (2015a)) show a significant effect of the isotropic hardening and the matrix elasticity on the resulting porosity ratcheting (i.e., void growth with increase of the number of cycles). Of equal importance to porosity ratcheting was also the stress triaxiality and the initial void shape. A possible interpretation is that porosity ratcheting is mainly a combined consequence of hardening and elasticity, which induce under finite strains an asymmetry in the void shape and porosity evolution. In turn, a closer look to the deformation of the void revealed a strong deviation from an ellipsoidal void shape (called ellipsoidicity deviation) at large number of cycles and axisymmetric loading states. This last observation could put into question the use of simplified homogenization and micromechanical models for porous materials with ellipsoidal voids. Yet, as we will see in this work, these models, although being approximate in terms of void shape description, can still provide qualitative and quantitative tools to analyze complex loading paths such as cyclic loads. Finally, in a very recent study, Lacroix et al. (2016) have analyzed in more detail the effect of elasticity and hardening in a spherical porous shell under different triaxial states and reached similar conclusions. In that work, based on an earlier model by Leblond et al. (1995), a first attempt to propose an improved Gurson model via radial discretization of an underlying spherical microcell at each material point was done.

In the present study, we use the linear comparison composite (LCC) homogenization method of Ponte Castañeda (1991) (see also Michel and Suquet (1992)) to extend the MVAR model of Danas and Aravas (2012) in the context of isotropic–linear kinematic hardening and cyclic loads. The present model, which deals with general ellipsoidal void shapes and orientations, uses a simplified decoupled homogenization strategy to separately deal with the elastic and plastic homogenization and proposes a complete set of evolution laws for the porosity, void shape and orientation during elastic and plastic loading, respectively. In turn, isotropic hardening is taken into account in a heuristic manner at the very end of the homogenization process, since such a procedure has been shown recently (Papadioti et al., 2016) to provide sufficiently accurate results not only for the macroscopic stress - strain response but also for the average strains in the inclusions.

It should be noted at this point that the decoupled homogenization strategy followed in the present work can in practice introduce errors in cyclic loads. These errors tend to be more important at large volume fractions of the inclusions or pores (Idiart and Lahellec, 2016) but they also tend to smear out at larger number of cycles. In the present study we deal with moderate porosities (less than 10%) and the errors due to the decoupling strategy are shown to be minor and negligible by comparison with the full field finite element results

obtained in the present paper. In other cases, however, that these errors could be large, the decoupling strategy should probably be used with caution. To amend this, recently, Lahellec and Suquet (2007) proposed an incremental variational formulation for materials with a hereditary behavior described by two potentials: a free energy and a dissipation function. This method has been introduced mainly to deal with the coupled elasto-plastic response of composites in an attempt to resolve the cyclic response of these materials (see also recent work by Brassart et al. (2011)). Note that these more advanced methods use the aforementioned or variants of the LCC estimates.

The aim of this paper is twofold. The first objective is to develop a homogenization model for porous materials (denoted as MVARX model henceforth) subjected to cyclic loads, where the elasticity contribution to the evolution of microstructure, the geometric anisotropy of the microstructure (void shapes and orientations) and the matrix hardening (isotropic and linear kinematic ones) can be simultaneously taken into account. The second objective is to assess the proposed model with full field multi-void computations by comparing the stress and porosity ratcheting response as a function of the number of cycles. More specifically, after a brief presentation of the microstructure (i.e. void geometry) and the matrix properties in Section 2, the instantaneous effective response is obtained in Section 3 both in the elastic and the plastic regime. Next, Section 4 discusses the microstructure evolution equations and defines the elasto-plastic incremental modulus. The numerical implementation of the present model into a user-material subroutine (UMAT) in Abaqus is discussed in Appendix A. The MVARX model is then assessed in Section 5 by comparison with results for ten and thirty cycles at finite strains obtained with the finite element method (FEM). Additional parametric studies for different types of cyclic loads (with no compression and initial pre-stress) are also carried using the MVARX model in Section 6 for up to hundred cycles. We finally conclude the present work with section 7.

2. Void geometry and local matrix response

This section deals with the modeling of a porous elasto-plastic material comprising ellipsoidal voids. In order to carry out the homogenization problem in Section 3, we first define the void geometry (i.e., microstructure) by introducing the relevant microstructural variables and then describe the local constitutive response of the phases.

2.1. Description of microstructure

Let us consider a porous material whose microstructure is taken to be statistically uniform and described by a representative volume element (RVE) (see Fig.1), denoted Ω. It is composed of the matrix $\Omega^{(1)}$ and the void space $\Omega^{(2)}$. Specifically, the matrix $\Omega^{(1)}$ is supposed to be made of an elastoplastic material with linear kinematic strain hardening, while the void phase is in the form of ellipsoids uniformly distributed in the matrix. Note that the voids $\Omega^{(2)}$ change their volumes, shapes and orientations under finite deformations, which leads to a deformation induced anisotropy. These variables are conveniently grouped by the set

$$\boldsymbol{s}_\alpha = \left\{ f, w_1, w_2, \boldsymbol{n}^{(1)}, \boldsymbol{n}^{(2)}, \boldsymbol{n}^{(3)} = \boldsymbol{n}^{(1)} \times \boldsymbol{n}^{(2)} \right\}. \tag{1}$$

The above variables are detailed below.

- Porosity $f = V^{(2)}/V$, where the total volume $V = V^{(1)} + V^{(2)}$ compose the matrix $V^{(1)}$ and the vacuous phase $V^{(2)}$.
- Two void aspect ratios $w_1 = a_3/a_1$ and $w_2 = a_2/a_1$, where $2a_i$, $(i = 1, 2, 3)$ denote the length of the principal axes of the representative ellipsoidal void (note that all voids have the same aspect ratios in this study).
- The void orientation unit vectors $\boldsymbol{n}^{(i)}$, $(i = 1, 2, 3)$ defining the orthogonal basis respectively coinciding with the principal axes of the representative ellipsoidal void (note that all voids have the same orientation in this study).

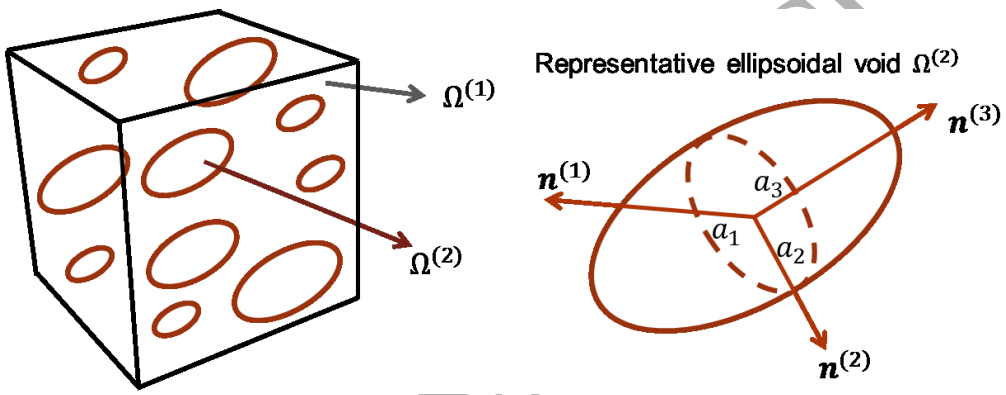

Figure 1: Representative volume element (RVE)

2.2. Local response of the matrix

In order to simplify the homogenization process, we initially neglect the isotropic hardening of the matrix phase which we will add in an ad-hoc manner at the final homogenized model in Section 3 [1]. This approximation has already been shown to be sufficiently accurate (Danas and Aravas, 2012; Cao et al., 2015; Papadioti et al., 2016). By contrast, linear kinematic hardening is introduced by use of an energy term and needs to be homogenized. The relevant variables needed for the matrix are thus the microscopic strain tensor $\boldsymbol{\varepsilon}$, the corresponding plastic one $\boldsymbol{\varepsilon}^p$ and a second order tensor $\boldsymbol{\alpha}$ representing the linear kinematic hardening variable.

Consequently, the Helmholtz free energy of the matrix material can be described by two quadratic potentials (see for instance Chaboche and Jung (1998)), one for the elastic energy and the other for the stored energy, i.e.,

$$\mathcal{W}(\boldsymbol{\varepsilon}^e, \boldsymbol{\alpha}) = \frac{1}{2}\boldsymbol{\varepsilon}^e : \mathbb{L}_e : \boldsymbol{\varepsilon}^e + \frac{1}{2}\boldsymbol{\alpha} : \mathbb{L}_X : \boldsymbol{\alpha} \tag{2}$$

[1] As is the usual practice in such problems, we first homogenize the elastic part using small strains and the viscoplastic part using a stress potential which can be related to an incremental strain-rate framework. Then, the homogenized problem is extended to a finite strain framework in Section 3.3.

Here, $\boldsymbol{\varepsilon}^e$ is the elastic strain tensor and $\mathbb{L}_e$ the elastic modulus tensor of the matrix phase which is the inverse of the elastic compliance tensor $\mathbb{M}_e$. They take the form

$$\mathbb{L}_e = \mathbb{M}_e^{-1}, \quad \mathbb{M}_e = \frac{1}{2\mu_e}\mathbb{K} + \frac{1}{3\kappa_e}\mathbb{J} \tag{3}$$

where μ_e and κ_e are the elastic shear and bulk moduli of the matrix, respectively. Recall also here the fourth order deviatoric projection tensor $\mathbb{K}$ or $K_{ijkl} = (\delta_{ik}\delta_{jl} + \delta_{il}\delta_{jk})/2 - \delta_{ij}\delta_{kl}/3$ and the hydrostatic projection tensor $\mathbb{J}$ or $J_{ijkl} = \delta_{ij}\delta_{kl}/3$, with δ_{ij} being the Cartesian components of the Kronecker delta.

In turn, the potential related to the kinematic hardening, is described here by an isotropic fourth-order tensor $\mathbb{L}_X$ named as the kinematic strain hardening modulus, such that

$$\mathbb{L}_X = \mathbb{M}_X^{-1}, \quad \mathbb{M}_X = \frac{1}{2\mu_X}\mathbb{K} + \frac{1}{3\kappa_X}\mathbb{J} \quad \text{with} \quad \mu_X = \frac{C}{3}, \quad \kappa_X \mapsto \infty \tag{4}$$

in which C is the kinematic hardening parameter (Prager, 1949) (see also Chaboche and Jung (1998); Chaboche (2008)). It is important to emphasize here that the kinematic hardening bulk modulus $\kappa_X \mapsto \infty$ due to the plastic incompressibility of matrix, but the limit must be taken after the homogenization is carried out, otherwise the effect of the porous phase will not be appropriately taken into account. $\boldsymbol{\alpha}$ in Eq.(2) is the tensorial internal variable descrbing kinematic hardening.

The constitutive law derived from Eq.(2) reads:

$$\boldsymbol{\sigma} = \frac{\partial \mathcal{W}}{\partial \boldsymbol{\varepsilon}^e} = \mathbb{L}_e : \boldsymbol{\varepsilon}^e, \qquad \boldsymbol{\chi} = \frac{\partial \mathcal{W}}{\partial \boldsymbol{\alpha}} = \mathbb{L}_X : \boldsymbol{\alpha} \tag{5}$$

where $\boldsymbol{\chi}$ is the microscopic (local) back stress tensor, which is deviatoric due to the incompressibility of the matrix.

Next, we describe the dissipative character of the rate-dependent plastic matrix phase by a stress dissipation (viscoplastic) potential, which takes the form

$$U(\boldsymbol{\sigma} - \boldsymbol{\chi}) = \frac{d_0\,\sigma_0}{n+1}\left[\frac{(\boldsymbol{\sigma} - \boldsymbol{\chi})_{eq}}{\sigma_0}\right]^{n+1}, \quad \text{with} \quad (\boldsymbol{\sigma} - \boldsymbol{\chi})_{eq} = \sqrt{\frac{3}{2}(\boldsymbol{s} - \boldsymbol{\chi}) : (\boldsymbol{s} - \boldsymbol{\chi})}. \tag{6}$$

Here, the scalars σ_0 and d_0 denote the flow stress of the matrix and a reference strain rate, $\boldsymbol{s}$ is the deviator of the microscopic (local) stress tensor.

Note that the viscoplastic nonlinearity of the matrix phase is characterized by the creep exponent n (i.e. strain-rate sensitivity parameter $m = 1/n$) and the homogenization model discussed in Section 3 is one for a general viscoplastic response and for any value of n. Nonetheless, the interest in this work is mainly on rate-independent plasticity, which implies taking the limit of $n \mapsto \infty$. This again will be considered after the homogenization procedure is carried out. In the rate-independent limit $n \mapsto \infty$, the stress potential in (6) becomes

$$U(\boldsymbol{\sigma} - \boldsymbol{\chi}) = \begin{cases} 0, & \text{if} \quad (\boldsymbol{\sigma} - \boldsymbol{\chi})_{eq}/\sigma_0 \leq 1 \\ \infty, & \text{otherwise} \end{cases} \tag{7}$$

which is the indicator function of the plastic domain in the case of the linear kinematic hardening yield condition (i.e. Prager model (Prager, 1949)) in the matrix, defined by

$$\Phi(\boldsymbol{\sigma}, \boldsymbol{\chi}) = (\boldsymbol{\sigma} - \boldsymbol{\chi})_{eq} - \sigma_0 \leq 0. \tag{8}$$

Using finally the yield condition (8), one obtains the constitutive laws for the corresponding strain-rate measures by considering an associated flow-rule

$$\dot{\boldsymbol{\varepsilon}}^p = \dot{\lambda} \frac{\partial \Phi}{\partial \boldsymbol{\sigma}}, \quad \dot{\boldsymbol{\alpha}} = -\dot{\lambda} \frac{\partial \Phi}{\partial \boldsymbol{\chi}} \quad \Rightarrow \quad \dot{\boldsymbol{\varepsilon}}^p = \dot{\boldsymbol{\alpha}}, \tag{9}$$

where the $\dot{(\cdot)}$ denotes time derivative.

3. Instantaneous effective response - decoupled homogenization

The main objective of this section is the description of the decoupled linear/non-linear homogenization procedure for the porous material described in Section 2. The effective (macroscopic) elastic and plastic behavior of the porous material will be treated independently at this level (see similar work in Aravas and Ponte Castañeda (2004) and Danas and Aravas (2012)). The independent treatment is of course an assumption, as discussed in detail by Lahellec and Suquet (2007), but as we will show later in the results section, it is a sufficiently accurate one for low to moderate porosities considered here. By decoupling elastic and plastic regions (similar to numerous earlier studies, e.g. one of the earliest ones Aravas (1987)), one can treat the homogenization of the elastic problem and the (visco)plastic problem separately. In the following, we first present briefly the homogenization of the elastic problem in small strains. Then, we describe the nonlinear homogenization of the (visco)plastic stress potential which can be related to a strain-rate (i.e., velocity gradient) dissipation potential. Finally, we assemble the two decoupled parts in a finite-strain framework by using objective co-rotational rates and microstructural spins. The numerical implementation of the presented homogenization model is detailed in Appendix A.

3.1. Effective free energy at small strains

In this subsection, we describe the homogenization of the free energy in Eq.(2). As mentioned before, we follow a decoupled strategy allowing to homogenize the two-potentials in (2) separately, neglecting then the coupling between them. This approach simplifies considerably the homogenization problem but of course introduces an error. Nevertheless, as we will see in the results section, this error is relatively minor for low to moderate porosity and is more present in the first cycle.

Consequently, the effective free energy reads

$$\widetilde{W}(\boldsymbol{E}_e, \boldsymbol{A}) = \frac{1}{2}\boldsymbol{E}_e : \widetilde{\mathbb{L}}_e : \boldsymbol{E}_e + \frac{1}{2}\boldsymbol{A} : \widetilde{\mathbb{L}}_X : \boldsymbol{A}, \tag{10}$$

where $\boldsymbol{E}_e$ is the effective elastic strain tensor and $\boldsymbol{A}$ the macroscopic counterpart of $\boldsymbol{\alpha}$. The effective elastic stiffness tensor, $\widetilde{\mathbb{L}}_e$, and the secant linear kinematic hardening modulus, $\widetilde{\mathbb{L}}_X$, respectively, become

$$\widetilde{\mathbb{L}}_e = \widetilde{\mathbb{M}}_e^{-1}, \quad \widetilde{\mathbb{M}}_e = \mathbb{M}_e + \frac{f}{1-f}\mathbb{Q}_e^{-1}, \tag{11}$$

and (for $\kappa_X \mapsto \infty$)

$$\widetilde{\mathbb{L}}_X = \widetilde{\mathbb{M}}_X^{-1}, \quad \widetilde{\mathbb{M}}_X = \frac{1}{2\mu_X}\mathbb{K} + \frac{f}{1-f}\mathbb{Q}_X^{-1}. \tag{12}$$

In these expressions, $\mathbb{Q}_e$ and $\mathbb{Q}_X$ are fourth order "compressible" (due to the void phase) microstructural tensors with both major and minor symmetries. They can be calculated from the Eshelby tensor $\mathbb{S}_e$ and $\mathbb{S}_X$, respectively (Eshelby, 1957; Mura, 1987) via

$$\mathbb{Q}_e(\mu_e, \kappa_e, w_1, w_2, \boldsymbol{n}^{(1)}, \boldsymbol{n}^{(3)}, \boldsymbol{n}^{(2)}) = \mathbb{L}_e : (\mathbb{I} - \mathbb{S}_e)\,. \tag{13}$$

and

$$\mathbb{Q}_X(\mu_X, \kappa_X, w_1, w_2, \boldsymbol{n}^{(1)}, \boldsymbol{n}^{(2)}, \boldsymbol{n}^{(3)}) = \lim_{\kappa_X \mapsto \infty} \mathbb{L}_X : (\mathbb{I} - \mathbb{S}_X) \tag{14}$$

Note again that the incompressibility limit $\kappa_X \mapsto \infty$ needs to be evaluated after the multiplication of the $\mathbb{L}_X$ with $(\mathbb{I} - \mathbb{S}_X)$.

The effective state law can be derived from the effective free energy (10), where $\boldsymbol{\Sigma}$ is the macroscopic stress tensor and $\boldsymbol{X}$ is the macroscopic back stress tensor:

$$\boldsymbol{\Sigma} = \frac{\partial \widetilde{W}}{\partial \boldsymbol{E}_e} = \widetilde{\mathbb{L}}_e : \boldsymbol{E}_e, \quad \boldsymbol{X} = \frac{\partial \widetilde{W}}{\partial \boldsymbol{A}} = \widetilde{\mathbb{L}}_X : \boldsymbol{A} \tag{15}$$

It should be emphasized here that the effective back stress tensor $\boldsymbol{X}$ has a nonzero compressible part since $\mathbb{L}_X$ is compressible.

3.2. Effective (visco)plastic potential

The effective (visco)plastic stress potential of the porous material is formally defined by

$$\widetilde{U}(\boldsymbol{\Sigma}, \boldsymbol{s}_\alpha) = \min_{\boldsymbol{\sigma} \in \mathcal{S}(\boldsymbol{\sigma})} \int_\Omega U(\boldsymbol{\sigma})\, dV = (1-f) \min_{\boldsymbol{\sigma} \in \mathcal{S}(\boldsymbol{\sigma})} \int_{\Omega^{(1)}} U^{(1)}(\boldsymbol{\sigma})\, dV \tag{16}$$

where $S(\boldsymbol{\sigma})$ represents the set of statically admissible stress field, i.e.,

$$\mathcal{S}(\boldsymbol{\sigma}) = \{\boldsymbol{\sigma}\,;\ \operatorname{div} \boldsymbol{\sigma} = \boldsymbol{0} \ \text{ in } \ \Omega, \quad \boldsymbol{\sigma} = 0 \ \text{ in } \ \Omega^{(2)}, \quad \boldsymbol{\sigma} \cdot \boldsymbol{n} = 0 \ \text{ on } \ \partial\Omega^{(2)}\}. \tag{17}$$

Following the work of Mbiakop et al. (2015b), which is based on the original method of Ponte Castañeda (1991), we introduce the approximate estimates for the effective stress potential

$$\widetilde{U}(\boldsymbol{\Sigma} - \boldsymbol{X}, \boldsymbol{s}_\alpha) \simeq \operatorname*{stat}_{\mu_p} \left\{ \widetilde{U}_L(\boldsymbol{\Sigma} - \boldsymbol{X}, \mu_p) - (1-f) \operatorname*{stat}_{\widehat{\boldsymbol{\sigma}-\boldsymbol{\chi}}} \left[U_L(\widehat{\boldsymbol{\sigma}-\boldsymbol{\chi}}, \mu_p) - U(\widehat{\boldsymbol{\sigma}-\boldsymbol{\chi}}) \right] \right\} \tag{18}$$

where $\widetilde{U}_L$ denotes the effective stress potential of a LCC and U_L describes the quadratic effective stress potential of the matrix in the LCC. In the present case, those read

$$U_L(\boldsymbol{\sigma} - \boldsymbol{\chi}, \mu_p) = \frac{1}{6\mu_p}(\boldsymbol{\sigma} - \boldsymbol{\chi})_{eq}^2, \tag{19}$$

$$\widetilde{U}_L(\boldsymbol{\Sigma}-\boldsymbol{X},\mu_p)=\frac{1}{2}(\boldsymbol{\Sigma}-\boldsymbol{X}):\widetilde{\mathbb{M}}_p(\mu_p):(\boldsymbol{\Sigma}-\boldsymbol{X}). \tag{20}$$

An improved expression of the effective plastic compliance tensor $\widehat{\mathbb{M}}_p$ for the linear comparison porous material (see Danas and Aravas (2012)) takes the form

$$\widetilde{\mathbb{M}}_p=\widetilde{\mathbb{M}}_p^{\text{var}}+(q_J^2-1)\mathbb{J}:\widetilde{\mathbb{M}}_p^{\text{var}}:\mathbb{J}, \tag{21}$$

with

$$\widetilde{\mathbb{M}}_p^{\text{var}}=\frac{3}{2\mu_p}\mathbb{K}+\frac{3f}{(1-f)\mu_p}\widehat{\mathbb{Q}}_p^{-1},\quad q_J=\frac{1-f}{\sqrt{f}\ln(1/f)}. \tag{22}$$

Readers are referred to the appendix of Cao et al. (2015) who provides explicit expressions for the evaluation of the tensor of $\widehat{\mathbb{Q}}_p$. Following Danas and Aravas (2012)), it is easily shown that $\widetilde{\mathbb{M}}_p$ is proportional to μ_p^{-1}. Therefore, by introducing a fourth order tensor which is homogeneous of degree zero in μ_p, e.g.,

$$\widehat{\mathbb{M}}_p=\mu_p\widetilde{\mathbb{M}}_p=\frac{3}{2}\mathbb{K}+\frac{3f}{(1-f)}\widehat{\mathbb{Q}}_p^{-1}+(q_J^2-1)\frac{3f}{(1-f)}\mathbb{J}:\widehat{\mathbb{Q}}_p^{-1}:\mathbb{J}, \tag{23}$$

the optimization with respect to μ_p in (18) is straightforward.

More specifically, inserting (19) and (20) into (18), and considering (6), one obtains

$$\begin{aligned}\widetilde{U}(\boldsymbol{\Sigma}-\boldsymbol{X},\boldsymbol{s}_\alpha)\simeq\underset{\mu_p}{\text{stat}}\Bigg[&\frac{1}{2\mu_p}(\boldsymbol{\Sigma}-\boldsymbol{X}):\widehat{\mathbb{M}}_p:(\boldsymbol{\Sigma}-\boldsymbol{X})\\&+(1-f)\underset{\widehat{\boldsymbol{\sigma}-\boldsymbol{\chi}}}{\text{stat}}\left(\frac{d_0\,\sigma_0}{n+1}\left(\frac{(\widehat{\boldsymbol{\sigma}-\boldsymbol{\chi}})_{eq}}{\sigma_0}\right)^{n+1}-\frac{1}{6\mu}(\widehat{\boldsymbol{\sigma}-\boldsymbol{\chi}})_{eq}^2\right)\Bigg].\end{aligned} \tag{24}$$

The first optimization operation in (24) with respect to $\widehat{\boldsymbol{\sigma}-\boldsymbol{X}}$ results in

$$d_0\left(\frac{(\widehat{\boldsymbol{\sigma}-\boldsymbol{\chi}})_{eq}}{\sigma_0}\right)^{n-1}=\frac{\sigma_0}{3\mu_p}. \tag{25}$$

Substitution of the above optimized expression (25) in (24) and optimization with respect to μ_p gives the optimized plastic modulus of the LCC as

$$\mu_p=\frac{\sigma_0^n}{3d_0}\left[\frac{1-f}{3(\boldsymbol{\Sigma}-\boldsymbol{X}):\widehat{\mathbb{M}}_p:(\boldsymbol{\Sigma}-\boldsymbol{X})}\right]^{\frac{n-1}{2}} \tag{26}$$

with $\widehat{\mathbb{M}}_p$ being derived in equation (23).

Finally, substitution of the above result in (24) leads to the final expression, called here MVARX (modified variational with linear kinematic hardening) model,

$$\widetilde{U}(\boldsymbol{\Sigma}-\boldsymbol{X},\boldsymbol{s}_\alpha)=(1-f)\frac{d_0\,\sigma_y(\bar{\varepsilon}^p)}{n+1}\left[\frac{3(\boldsymbol{\Sigma}-\boldsymbol{X}):\widehat{\mathbb{M}}_p:(\boldsymbol{\Sigma}-\boldsymbol{X})}{(1-f)\,\sigma_y^2(\bar{\varepsilon}^p)}\right]^{\frac{n+1}{2}}. \tag{27}$$

In this expression, we have heuristically replaced σ_0 with $\sigma_y(\bar{\varepsilon}^p)$ to allow for a general isotropic hardening, as $\bar{\varepsilon}^p$ denotes the accumulated (creep) plastic strain in the matrix phase. This is done approximately here since the homogenization process was carried out for a matrix with no isotropic hardening. Nonetheless, in numerous recent studies (see for instance Cao et al. (2015) and Papadioti et al. (2016)), this approximation was shown to deliver very accurate results and thus is used here as well. In the present study, the instantaneous yield stress σ_y of the matrix phase is expressed in terms of the initial yield stress σ_0, the initial yield strain ε_0 of the matrix material and the isotropic hardening exponent N, as

$$\sigma_y = \sigma_0 \left(1 + \frac{\bar{\varepsilon}^p}{\varepsilon_0}\right)^{1/N}, \quad \varepsilon_0 = \frac{\sigma_0}{E}. \tag{28}$$

Any other isotropic hardening law for the matrix could be used without incurring any changes in the homogenized model .

Next, in order to obtain a yield criterion in the rate independent limit, it suffices to consider the limit $n \mapsto \infty$ in (27). This readily leads to the effective yield condition for the porous material

$$\widetilde{\Phi}(\boldsymbol{\Sigma} - \boldsymbol{X}, \boldsymbol{s}_\alpha) = \frac{3(\boldsymbol{\Sigma} - \boldsymbol{X}) : \widehat{\mathbb{M}}_p : (\boldsymbol{\Sigma} - \boldsymbol{X})}{1 - f} - \sigma_y^2(\bar{\varepsilon}^p) = 0. \tag{29}$$

3.3. Extension to finite strains

In this section, we extend the previous set of equations in the context of finite strains and objective co-rotational stress rates. The macroscopic strain-rate tensor $\boldsymbol{D}$ of the homogenized porous material are classically assumed to be the sum of the elastic part $\boldsymbol{D}_e$ and the plastic one $\boldsymbol{D}_p$ so that

$$\boldsymbol{D} = \boldsymbol{D}_e + \boldsymbol{D}_p. \tag{30}$$

Next, by refering to the effective elastic energy (10), we assume the effective hypoelastic response Aravas and Ponte Castañeda (2004)

$$\boldsymbol{D}_e = \widetilde{\mathbb{M}}_e : \overset{\circ}{\boldsymbol{\Sigma}}, \quad \text{with} \quad \overset{\circ}{\boldsymbol{\Sigma}} = \dot{\boldsymbol{\Sigma}} - \boldsymbol{\omega} \cdot \boldsymbol{\Sigma} + \boldsymbol{\Sigma} \cdot \boldsymbol{\omega}, \tag{31}$$

and similarly

$$\overset{\circ}{\boldsymbol{X}} = \widetilde{\mathbb{L}}_X : \dot{\boldsymbol{A}} = \widetilde{\mathbb{L}}_X : \boldsymbol{D}_p, \quad \text{with} \quad \overset{\circ}{\boldsymbol{X}} = \dot{\boldsymbol{X}} - \boldsymbol{\omega} \cdot \boldsymbol{X} + \boldsymbol{X} \cdot \boldsymbol{\omega}, \tag{32}$$

where we will show later in Eq.(33) that $\dot{\boldsymbol{A}} = \boldsymbol{D}_p$. The effective back stress $\boldsymbol{X}$ has a non-zero hydrostatic part and depends on the porosity, void shape and orientation as a consequence of the compressible $\widetilde{\mathbb{L}}_X$ tensor. This is of course due to the homogenization of the corresponding potential energy for the kinematic hardening in equation (10). In the last two expressions, the superscript $(^\circ)$ denotes rates that are co-rotational with the microstructure (i.e., void anisotropy), which is measured by the so-called microscopic spin of the voids $\boldsymbol{\omega}$ (or the microstructural spin which is a skew symmetric second order tensor) (Aravas and Ponte Castañeda, 2004) to be defined formally in the following section.

Finally, since the matrix obeys an associated plastic flow rule, the homogenized porous material does too (Rice, 1971) in the plastic regime. As a result, the effective plastic strain-rate and effective hardening variable $\boldsymbol{A}$ (conjugate measure to the effective back stress $\boldsymbol{X}$) are simply

$$\boldsymbol{D}_p = \dot{\Lambda}\frac{\partial\widetilde{\Phi}}{\partial\boldsymbol{\Sigma}} = \dot{\Lambda}\,\boldsymbol{N}, \qquad \dot{\boldsymbol{A}} = -\dot{\Lambda}\frac{\partial\widetilde{\Phi}}{\partial\boldsymbol{X}} = \boldsymbol{D}_p \tag{33}$$

$\boldsymbol{D}_p = \dot{\boldsymbol{A}}$ is a direct consequence of the dependency of the effective stress potential on $\boldsymbol{\Sigma}-\boldsymbol{X}$.

4. Microstructure evolution

In this section, we write down the evolution laws for all the microstructural variables described in the context of relation (1) (see Fig.1). Those include the porosity f, the shape of the voids, described by the two aspect ratios w_1 and w_2, and the orientation of the principal axes of the representative ellipsoidal void $\boldsymbol{n}^{(i)}$ (with $n = 1, 2, 3$). Moreover, as it will become apparent in the results sections, we provide evolution equations for the above-mentioned variables not only during plastic loading as is the usual practice in porous solids but also during elastic loading. Since the strategy followed in this work is to decouple the elastic and plastic homogenization problems, it is natural that the same procedure may be used in the context of microstructure evolution. In other words, the microstructural variables $\boldsymbol{s}_\alpha$ evolve in the elastic regime due to the purely elastic strains and in the plastic regime due to the plastic strains. Henceforth, all subscripts "e" refer to elastic quantities and "p" to plastic quantities, respectively.

4.1. Evolution laws in elastic regime

In this section, we provide all the necessary quantities needed to evaluate the evolution of the void microstructure in the context of linear elasticity. In this regard, the estimation of the phase average elastic strain-rate fields, $\boldsymbol{D}_e^{(1)}$ in the matrix phase and $\boldsymbol{D}_e^{(2)}$ in the void phase, are given in terms of the strain-rate concentration tensors by (Hill, 1963; Laws, 1973; Willis, 1981)

$$\boldsymbol{D}_e^{(1)} = \mathbb{A}_e^{(1)} : \boldsymbol{D}_e, \quad \boldsymbol{D}_e^{(2)} = \mathbb{A}_e^{(2)} : \boldsymbol{D}_e, \quad (1-f)\boldsymbol{D}_e^{(1)} + f\boldsymbol{D}_e^{(2)} = \boldsymbol{D}_e \tag{34}$$

where the strain rate concentration tensor (or the localization tensor) denoted as $\mathbb{A}_e^{(r)}$ ($r = 1, 2$) read

$$\mathbb{A}_e^{(1)} = \frac{1}{1-f}\mathbb{M}_e : \widetilde{\mathbb{L}}_e, \quad \mathbb{A}_e^{(2)} = \frac{1}{f}\left[\mathbb{I} - \mathbb{M}_e : \widetilde{\mathbb{L}}_e\right], \quad (1-f)\mathbb{A}_e^{(1)} + f\mathbb{A}_e^{(2)} = \mathbb{I}. \tag{35}$$

Here, $\mathbb{M}_e$ and $\widetilde{\mathbb{L}}_e$ are given by Eqs. (3) and (12), respectively. Note also that $\mathbb{A}_e^{(r)}(r = 1, 2)$ are fourth-order tensors that exhibit minor symmetry (but not necessarily major symmetry).

Corresponding expressions have been introduced by Ponte Castañeda (1997) (see also Kailasam and Ponte Castañeda (1998)) for the evaluation of the average spin tensors in the vacuous phase, such that

$$\boldsymbol{W}_e^{(2)} = \boldsymbol{W}_e - \mathbb{C}_e : \boldsymbol{D}_e, \quad \mathbb{C}_e = -(1-f)\mathbb{T}_e : \mathbb{A}_e^{(2)}, \tag{36}$$

where $\mathbb{T}_e$ is the fourth order Eshelby rotation tensor[2] depending on the aspect ratios w_1, w_2 and the orientation vectors $\boldsymbol{n}^{(1)}$, $\boldsymbol{n}^{(2)}$, $\boldsymbol{n}^{(3)}$, $\mathbb{C}_e$ is skew-symmetric in the first two indices and symmetric in the last two ones, and $\boldsymbol{W}_e$ is the macroscopic elastic spin tensor.

Following the definition of the elastic concentration tensors $\mathbb{A}_e^{(2)}$ and $\mathbb{C}_e$, the elastic contribution to the microstructure evolution, $\dot{\boldsymbol{s}}_\alpha$, becomes:

- for the porosity evolution

$$\dot{f}_e = f\ \left[\mathrm{tr}(\boldsymbol{D}_e^{(2)}) - \mathrm{tr}(\boldsymbol{D}_e)\right]. \tag{37}$$

- for the two void aspect ratios evolution,

$$\begin{aligned}(\dot{w_e})_1 &= (w_e)_1 \left(\boldsymbol{n}_e^{(3)} \otimes \boldsymbol{n}_e^{(3)} - \boldsymbol{n}_e^{(1)} \otimes \boldsymbol{n}_e^{(1)}\right) : \mathbb{A}_e^{(2)} : \boldsymbol{D}_e \\ (\dot{w_e})_2 &= (w_e)_2 \left(\boldsymbol{n}_e^{(3)} \otimes \boldsymbol{n}_e^{(3)} - \boldsymbol{n}_e^{(2)} \otimes \boldsymbol{n}_e^{(2)}\right) : \mathbb{A}_e^{(2)} : \boldsymbol{D}_e\end{aligned} \tag{38}$$

- for the void orientation unit vectors,

$$\dot{\boldsymbol{n}}_e^{(i)} = \boldsymbol{\omega}_e \cdot \boldsymbol{n}_e^{(i)}, \qquad i = 1, 2, 3, \tag{39}$$

where $\boldsymbol{\omega}_e$ is the elastic part of the microstructural spin tensor, which is skew-symmetric and reads

$$\begin{aligned}\boldsymbol{\omega}_e =& \boldsymbol{W}_e - [\mathbb{C}_e : \boldsymbol{D}_e - \\ & \frac{1}{2} \sum_{i,j=1,\ i\neq j}^{3} \frac{(w_e)_i^2 + (w_e)_j^2}{(w_e)_i^2 - (w_e)_j^2} \left[\left(\boldsymbol{n}_e^{(i)} \otimes \boldsymbol{n}_e^{(j)} + \boldsymbol{n}_e^{(j)} \otimes \boldsymbol{n}_e^{(i)}\right) : \mathbb{A}_e^{(2)} : \boldsymbol{D}_e\right] \left(\boldsymbol{n}_e^{(i)} \otimes \boldsymbol{n}_e^{(j)}\right) \Bigg].\end{aligned} \tag{40}$$

In the same line of thought with the plastic spin (Dafalias, 1985), one could introduce the "elastic spin" $\boldsymbol{W}_e^E = \boldsymbol{W}_e - \boldsymbol{\omega}_e$, which is used to defined the spin of the continuum relative to the microstructure when the porous material is under elastic loading. One has then

$$\boldsymbol{W}_e^E = \mathbb{C}_e : \boldsymbol{D}_e - \frac{1}{2} \sum_{i,j=1,\ i\neq j}^{3} \frac{(w_e)_i^2 + (w_e)_j^2}{(w_e)_i^2 - (w_e)_j^2} \left[\left(\boldsymbol{n}_e^{(i)} \otimes \boldsymbol{n}_e^{(j)} + \boldsymbol{n}_e^{(j)} \otimes \boldsymbol{n}_e^{(i)}\right) : \mathbb{A}_e^{(2)} : \boldsymbol{D}_e\right] \left(\boldsymbol{n}_e^{(i)} \otimes \boldsymbol{n}_e^{(j)}\right). \tag{41}$$

4.2. Evolution laws in the plastic regime

A brief review of the plasticity contribution to the microstructure evolution is given in this section. Following the work of Ponte Castañeda and Zaidman (1994) and Ponte Castañeda and Suquet (1998) (see also Aravas and Ponte Castañeda (2004)), we first define

[2]The tensor $\mathbb{T}_e$ can be found in Mura (1987) or in the appendix of Aravas and Ponte Castañeda (2004) denoted with the symbol $\boldsymbol{\Pi}$.

the evolution of the accumulated plastic strain $\bar{\varepsilon}^p$ which is used to describe the isotropic hardening in the matrix phase (see Eq.(29)). Specifically, one can obtain the evolution law for $\bar{\varepsilon}^p$ by setting the macroscopic plastic work equal to the microscopic one, such that

$$(\boldsymbol{\Sigma} - \boldsymbol{X}) : \boldsymbol{D}_p = (1-f)\sigma_y(\bar{\varepsilon}^p)\,\dot{\bar{\varepsilon}}^p. \tag{42}$$

Considering the macroscopic flow rule (33), one has then

$$\dot{\bar{\varepsilon}}^p = \dot{\Lambda}\frac{(\boldsymbol{\Sigma} - \boldsymbol{X}) : \boldsymbol{N}}{(1-f)\sigma_y(\bar{\varepsilon}^p)} = \dot{\Lambda}\, g_1(\boldsymbol{\Sigma} - \boldsymbol{X}, \boldsymbol{s}_\alpha) \tag{43}$$

where $\boldsymbol{N}$ denotes the direction of the plastic flow and has been defined in (33) while g_1 is a homogeneous function of degree zero in $\dot{\Lambda}$.

Next, the plastic strain rate and plastic spin concentration tensors take the following form (Danas and Aravas, 2012)

$$\mathbb{A}_p^{(1)} = \frac{3}{2(1-f)}\mathbb{K} : \widehat{\mathbb{M}}_p^{-1}, \quad \mathbb{A}_p^{(2)} = \frac{1}{f}\left[\mathbb{I} - \frac{3}{2}\mathbb{K} : \widehat{\mathbb{M}}_p^{-1}\right], \quad \mathbb{C}_p = -(1-f)\mathbb{T}_p : \mathbb{A}_p^{(2)} \tag{44}$$

where $\widehat{\mathbb{M}}_p$ has been defined by equations (21), (22) and (23), while the plastic Eshelby rotation tensor $\mathbb{T}_p$ is given in Aravas and Ponte Castañeda (2004) or Cao et al. (2015) (denoted with the symbol $\boldsymbol{\Pi}$ in those references).

The microstructure evolution laws are then given as follows:

- *Porosity.* Taking into account matrix incompressibility during plastic loading, the corresponding evolution law for the porosity is obtained from the kinematic relations

$$\dot{f}_p = \alpha_f(1-f)\,\mathrm{tr}(\boldsymbol{D}_p) = \dot{\Lambda}\alpha_p(1-f)\mathrm{tr}(\boldsymbol{N}) = \dot{\Lambda}\, g_2(\boldsymbol{\Sigma} - \boldsymbol{X}, \boldsymbol{s}_\alpha) \tag{45}$$

  where g_2 is a scalar homogeneous function of degree zero in $\dot{\Lambda}$ and $\alpha_f(f_0)$ is a calibration function of the initial porosity f_0 introduced to enhance the accuracy of the initial porosity effect on the void growth. In the present work, we use

$$\alpha_f(f_0) = a f_0^2 + b f_0 + c,$$

  with $a = 42.80$, $b = -2.69$ and $c = 1.04$, which are obtained from the least squares method by considering the FEM computations carried out in this work.[3]

- *Aspect ratios.* The plastic contribution to the evolution of the aspect ratios of the ellipsoidal voids is defined by

$$\begin{aligned}(\dot{w}_p)_1 &= \alpha_w(w_p)_1\left(\boldsymbol{n}_p^{(3)}\otimes\boldsymbol{n}_p^{(3)} - \boldsymbol{n}_p^{(1)}\otimes\boldsymbol{n}_p^{(1)}\right) : \mathbb{A}_p^{(2)} : \boldsymbol{D}_p = \dot{\Lambda}\, g_3(\boldsymbol{\Sigma} - \boldsymbol{X}, \boldsymbol{s}_\alpha)\\ (\dot{w}_p)_2 &= \alpha_w(w_p)_2\left(\boldsymbol{n}_p^{(3)}\otimes\boldsymbol{n}_p^{(3)} - \boldsymbol{n}_p^{(2)}\otimes\boldsymbol{n}_p^{(2)}\right) : \mathbb{A}_p^{(2)} : \boldsymbol{D}_p = \dot{\Lambda}\, g_4(\boldsymbol{\Sigma} - \boldsymbol{X}, \boldsymbol{s}_\alpha)\end{aligned} \tag{46}$$

[3]It should be noted here that from a practical and engineering point of view, α_f could also be calibrated from direct experimental measurements but this is not further pursued here.

g_3 and g_4 are scalar homogeneous functions of degree zero in $\dot{\Lambda}$ while the scalar factor $\alpha_w = 1.75$ has been introduced similar to the original MVAR model (Danas and Aravas, 2012) to improve the corresponding prediction of the void shape evolution, but could be seen more generally as a calibration parameter.

- *Void orientation vectors.* The evolution of the orientation vectors due to plastic strains reads

$$\dot{\boldsymbol{n}}_p^{(i)} = \boldsymbol{\omega}_p \cdot \boldsymbol{n}_p^{(i)}, \qquad i = 1, 2, 3 \tag{47}$$

with

$$\begin{aligned}\boldsymbol{\omega}_p =& \boldsymbol{W}_p - \dot{\Lambda}\,[\mathbb{C}_p : \boldsymbol{N} \\ &-\frac{1}{2}\sum_{i,j=1,\ i\neq j}^{3} \frac{(w_p)_i^2 + (w_p)_j^2}{(w_p)_i^2 - (w_p)_j^2}\left[\left(\boldsymbol{n}_p^{(i)}\otimes\boldsymbol{n}_p^{(j)} + \boldsymbol{n}_p^{(j)}\otimes\boldsymbol{n}_p^{(i)}\right) : \mathbb{A}_p^{(2)} : \boldsymbol{N}\right]\boldsymbol{n}_p^{(i)}\otimes\boldsymbol{n}_p^{(j)}\Big]\end{aligned} \tag{48}$$

Using further the well known definition of the "plastic spin" (Dafalias, 1985) as $\boldsymbol{W}_p^P = \boldsymbol{W}_p - \boldsymbol{\omega}_p = \dot{\Lambda}\boldsymbol{\Omega}^P$, one can rewrite equation (48) as

$$\boldsymbol{\Omega}^P = \mathbb{C}_p : \boldsymbol{N} - \frac{1}{2}\sum_{i,j=1,\ i\neq j}^{3} \frac{(w_p)_i^2 + (w_p)_j^2}{(w_p)_i^2 - (w_p)_j^2}\left[\left(\boldsymbol{n}_p^{(i)}\otimes\boldsymbol{n}_p^{(j)} + \boldsymbol{n}_p^{(j)}\otimes\boldsymbol{n}_p^{(i)}\right) : \mathbb{A}_p^{(2)} : \boldsymbol{N}\right]\boldsymbol{n}_p^{(i)}\otimes\boldsymbol{n}_p^{(j)} \tag{49}$$

Note that $\boldsymbol{W}_p^P$ describes the spin of the continuum relative to the microstructure when the porous material is under purely plastic loading. Alternative expressions that describe the evolution of the void aspect ratios and the orientation vectors, that are not singular for spherical or spheroidal void shapes, have been recently proposed by Madou et al. (2013) and could be used readily used in the present model.

4.3. Elasto-plastic Jacobian

In order to implement numerically the present constitutive model, it is useful to evaluate at this point the elasto-plastic Jacobian, denoted by $\mathbb{L}^{ep}$. Using Jaumann objective measures, the general form of the macroscopic constitutive law can be written as (Aravas and Ponte Castañeda, 2004)

$$\overset{\triangledown}{\boldsymbol{\Sigma}} = \mathbb{L}^{ep} : \boldsymbol{D}. \tag{50}$$

The Jaumann rates $\overset{\triangledown}{\boldsymbol{\Sigma}}$ and $\overset{\triangledown}{\boldsymbol{X}}$ can also be obtained from the co-rotational Cauchy stress rate tensor $\overset{\circ}{\boldsymbol{\Sigma}}$ and back stress tensor $\overset{\circ}{\boldsymbol{X}}$ as a function of the plastic spin $\boldsymbol{W}_p^P$, i.e.,

$$\overset{\triangledown}{\boldsymbol{\Sigma}} = \overset{\circ}{\boldsymbol{\Sigma}} + \boldsymbol{\Sigma}\cdot\boldsymbol{W}_p^P - \boldsymbol{W}_p^P\cdot\boldsymbol{\Sigma}, \qquad \overset{\triangledown}{\boldsymbol{X}} = \overset{\circ}{\boldsymbol{X}} + \boldsymbol{X}\cdot\boldsymbol{W}_p^P - \boldsymbol{W}_p^P\cdot\boldsymbol{X} \tag{51}$$

while, using equation (31), the Cauchy stress co-rotational with the microstructure can be written as

$$\overset{\circ}{\boldsymbol{\Sigma}} = \widetilde{\mathbb{L}}_e : (\boldsymbol{D} - \boldsymbol{D}_p) = \widetilde{\mathbb{L}}_e : \boldsymbol{D} - \dot{\Lambda}\widetilde{\mathbb{L}}_e : \boldsymbol{N}. \tag{52}$$

In this last equation, the plastic multiplier $\dot{\Lambda}$ can be calculated from the consistency condition $\dot{\Phi} = 0$, as

$$\dot{\widetilde{\Phi}} = \frac{\partial \widetilde{\Phi}}{\partial \boldsymbol{\Sigma}} : \overset{\circ}{\boldsymbol{\Sigma}} + \frac{\partial \widetilde{\Phi}}{\partial \boldsymbol{X}} : \overset{\circ}{\boldsymbol{X}} + \frac{\partial \widetilde{\Phi}}{\partial \bar{\varepsilon}^p}\, \dot{\bar{\varepsilon}}^p + \frac{\partial \widetilde{\Phi}}{\partial \boldsymbol{s}_\alpha} \cdot \overset{\circ}{\boldsymbol{s}}_\alpha = 0, \tag{53}$$

where $\boldsymbol{s}_\alpha$ denotes the set of the microstructural variables defined in (1) and by use of (47), one readily gets $\overset{\circ}{\boldsymbol{n}}{}^{(i)} = 0$. It is recalled that the co-rotational back stress rate has been defined in equation (32).

Remark: For completeness, the Jaumann rates of the microstructural variables $\overset{\triangledown}{\boldsymbol{s}}_\alpha$ are given as follows (see also (Aravas and Ponte Castañeda, 2004))

$$\overset{\triangledown}{\boldsymbol{s}}_\alpha = \left\{ \overset{\triangledown}{f} = \dot{f}, \quad \overset{\triangledown}{w}_1 = \dot{w}_1, \quad \overset{\triangledown}{w}_2 = \dot{w}_2, \quad \overset{\triangledown}{\boldsymbol{n}}{}^{(i)} = -\dot{\Lambda} \boldsymbol{\Omega}^P \boldsymbol{n}^{(i)} \right\}$$

As a result, taking into account (33), the consistency condition (53) can be recast into

$$\boldsymbol{N} : (\overset{\circ}{\boldsymbol{\Sigma}} - \overset{\circ}{\boldsymbol{X}}) + \frac{\partial \widetilde{\Phi}}{\partial \bar{\varepsilon}^p}\, \dot{\bar{\varepsilon}}^p + \frac{\partial \widetilde{\Phi}}{\partial f}\, \dot{f} + \frac{\partial \widetilde{\Phi}}{\partial w_1}\, \dot{w}_1 + \frac{\partial \widetilde{\Phi}}{\partial w_2}\, \dot{w}_2 = 0. \tag{54}$$

Recall at this point that $\dot{\bar{\varepsilon}}^p = \dot{\Lambda} g_1$, $\dot{f}^p = \dot{\Lambda} g_2$, $\dot{w}_1^p = \dot{\Lambda} g_3$ and $\dot{w}_2^p = \dot{\Lambda} g_4$ (see also Eqs.(45) - (46)). Then, by introducing

$$H = -\left(\frac{\partial \widetilde{\Phi}}{\partial \bar{\varepsilon}^p}\, g_1 + \frac{\partial \widetilde{\Phi}}{\partial f}\, g_2 + \frac{\partial \widetilde{\Phi}}{\partial w_1}\, g_3 + \frac{\partial \widetilde{\Phi}}{\partial w_2}\, g_4 \right) \tag{55}$$

equation (54) becomes

$$\boldsymbol{N} : (\overset{\circ}{\boldsymbol{\Sigma}} - \overset{\circ}{\boldsymbol{X}}) - \dot{\Lambda} H = 0. \tag{56}$$

Next, inserting (32) and (51) into equation (56), one has

$$\boldsymbol{N} : \widetilde{\mathbb{L}}_e : \boldsymbol{D} - \dot{\Lambda} \cdot \boldsymbol{N} : \widetilde{\mathbb{L}}_e : \boldsymbol{N} - \dot{\Lambda} \cdot \boldsymbol{N} : \widetilde{\mathbb{L}}_X : \boldsymbol{N} - \dot{\Lambda} \cdot H = 0, \tag{57}$$

and the plastic multiplier can be readily obtained as

$$\dot{\Lambda} = \frac{\boldsymbol{N} : \widetilde{\mathbb{L}}_e : \boldsymbol{D}}{L}, \quad L = \boldsymbol{N} : \widetilde{\mathbb{L}}_e : \boldsymbol{N} + \boldsymbol{N} : \widetilde{\mathbb{L}}_X : \boldsymbol{N} + H. \tag{58}$$

Combining (51), (52) and (58), the Jaumann rate of the stress tensor can be explicitly expressed as

$$\overset{\triangledown}{\boldsymbol{\Sigma}} = \left[\widetilde{\mathbb{L}}_e - \frac{(\widetilde{\mathbb{L}}_e : \boldsymbol{N}) \otimes (\boldsymbol{N} : \widetilde{\mathbb{L}}_e)}{L} + \frac{\boldsymbol{N} : \widetilde{\mathbb{L}}_e}{L} \otimes (\boldsymbol{\Sigma} \cdot \boldsymbol{\Omega}^P - \boldsymbol{\Omega}^P \cdot \boldsymbol{\Sigma}) \right] : \boldsymbol{D} \tag{59}$$

from which we obtain the elasto-plastic Jacobian

$$\mathbb{L}^{ep} = \widetilde{\mathbb{L}}_e - \frac{(\widetilde{\mathbb{L}}_e : \boldsymbol{N}) \otimes \boldsymbol{N} : (\widetilde{\mathbb{L}}_e)}{L} + \frac{\boldsymbol{N} : \widetilde{\mathbb{L}}_e}{L} \otimes (\boldsymbol{\Sigma} \cdot \boldsymbol{\Omega}^P - \boldsymbol{\Omega}^P \cdot \boldsymbol{\Sigma}) \tag{60}$$

This last expression has the same structure as the corresponding one in Aravas and Ponte Castañeda (2004) with the only difference lying in the expression of L defined in equation (58), which is augmented with the linear kinematic hardening modulus $\widetilde{\mathbb{L}}_X$ and the fact that the normal $\boldsymbol{N} = \boldsymbol{N}(\boldsymbol{\Sigma} - \boldsymbol{X})$. The numerical implementation of the model is described in Appendix A.

5. Assessment of the MVARX model with FEM simulations

In this section, the predictions of the MVARX model are assessed by comparison to FEM simulations for cyclic loadings and finite strains. To this end, the MVARX model is implemented in a user-defined material subroutine (UMAT) in ABAQUS/Standard software. The homogenized elasto-plastic constitutive equations are integrated at each Gauss point of a single cubic 8-node element, which serves immediately as a representative volume element. Note that the isotropic and kinematic hardening are fully characterized by the hardening exponent N and hardening modulus C (see equations (6) and (4)), as well as the Young's modulus E of the matrix phase.

In turn, for the FEM simulations, we use periodic unit cells comprising uniformly distributed voids. This is achieved by use of an Random Sequential Adsorption (RSA) algorithm as described in Lopez-Pamies et al. (2013). In Fig.2, we show three different realizations comprising 30 monodisperse voids with a total initial porosity $f_0 = 5\%$[4]. The comparison between the MVARX model and the FEM is done for the average macroscopic stress and porosity.

[4]It should be pointed out here that the MVARX estimations and FEM computations are realized by considering the porous material only with initial spherical voids but of course allow for void shape evolution during the deformation process. The initial void shape effects have been shown to have a significant effect on the cyclic response (Mbiakop et al., 2015a) but in the present study we choose to focus on the rest of the parameters of the problem and concentrate the study on porosity ratcheting only.

(a) (b) (c)

Figure 2: Geometries and meshes of three different realizations comprising 30 voids with a total initial porosity $f_0 = 5\%$.

Specifically, in this section, we consider a uniaxial tension/compression cyclic loading, as shown schematically in Fig.3. In each step of each cycle, we control the average nominal strain $E_{22} = U_2/L$ in the unit-cell (U_2 is the axial applied displacement and L the initial side length of the RVE cube), which initially increases from $E_{22} = 0$ to $E_{22} = 0.05$ (the later corresponds to the maximal imposed displacement U_{max}), then unloads from $E_{22} = 0.05$ to $E_{22} = 0$, next reversely loads from $E_{22} = 0$ to $E_{22} = -0.05$ and finally unloads from $E_{22} = -0.05$ to $E_{22} = 0$. The number of cycles is denoted as N_r. In addition, the matrix material has a Young modulus $E/\sigma_0 = 300$, a Poisson ratio $\nu = 0.3$ and an initial porosity $f_0 = 0.05$, unless otherwise stated.

More specifically, section 5.1 investigates first the detailed response of MVARX in the case of two cycles. As expected, the influence of the matrix hardening on the effective constitutive relation $\Sigma_{22} - E_{22}$ and on the porosity evolution are clearly illustrated and validated. This effect is also discussed in section 5.2 in the case of 10 cycles. In the remaining sections 5.3 to 5.4 we study the effect of the Young modulus of the matrix material, the matrix elasticity contribution and the initial porosity f_0 upon the effective cyclic response of the porous material.

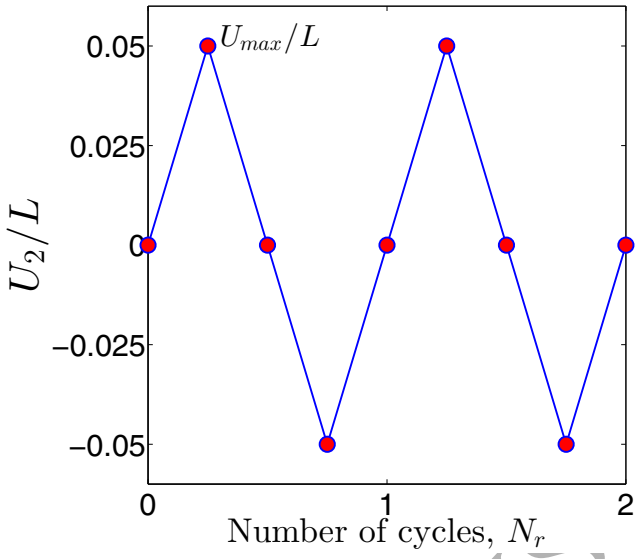

Figure 3: Schematic explanation of the uniaxial "traction-compression" cyclic loading

5.1. Detailed response for 2 cycles

In Fig.4, we show comparisons between the MVARX model and the FEM for combined isotropic and kinematic hardening with $N = 10$ and $C/\sigma_0 = 10$ for two complete cycles. In Fig.4(a), we observe that the agreement between the MVARX predictions and the numerical results for the effective stress-strain response $\Sigma_{22} - E_{22}$ is very good for the entire loading history. The effects of the isotropic and kinematic hardening are well predicted in the present case. A slight difference is observed in the inset of that figure exactly at the elasto-plastic transition. This difference, as already mentioned above, is due to the decoupled homogenization strategy used in section 3. This difference is of course minor and thus justifies to keep the present approximation. In turn, Fig.4(b) shows the evolution of porosity f as a function of the nominal axial strain E_{22}. The MVARX model tends to overestimate the porosity evolution as already observed in previous studies (see for instance Cao et al. (2015)) but qualitatively captures the increase of porosity at the second cycle. For that, one only needs to follow the value of porosity at $E_{22} = 0.05$ after one and two cycles. Both the MVARX and the FEM predict porosity ratcheting (see relevant numerical results of Mbiakop et al. (2015a)), which is a highly non-trivial qualitative feature of the model. In the following parts of this section, we switch to plots for larger numbers of cycles $N_r = 10$ or 30 in order to assess mainly the qualitative performance of the model with respect to the FEM results.

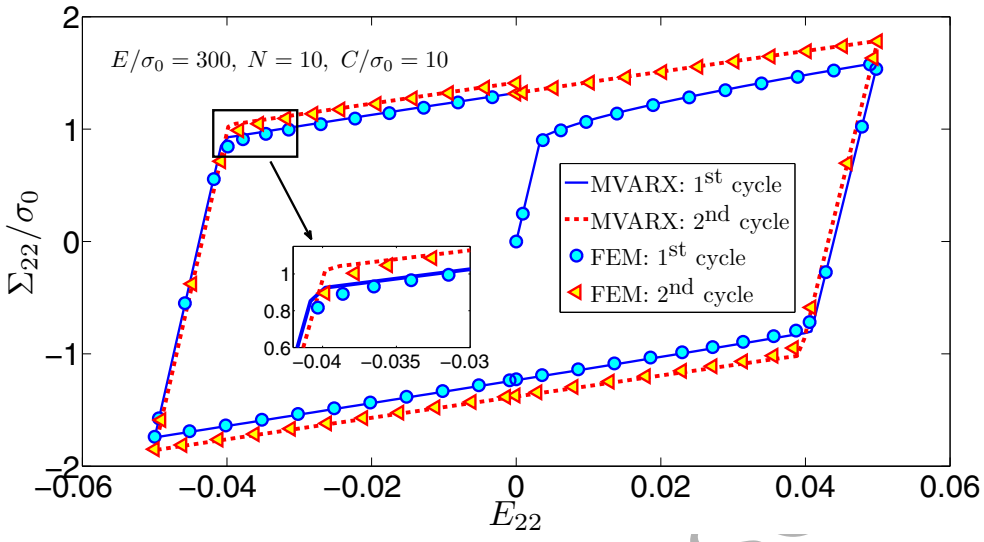

(a)

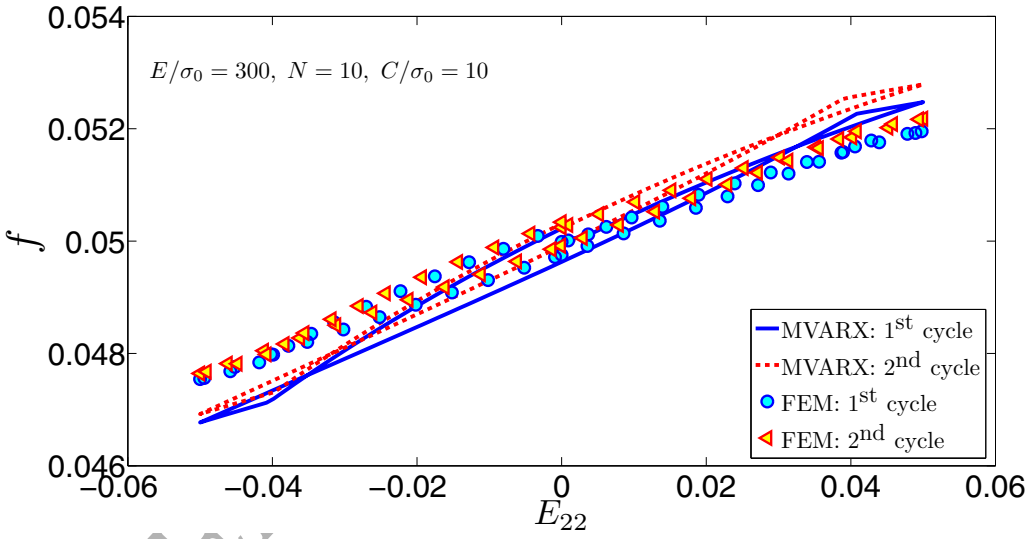

(b)

Figure 4: Comparison of MVARX model predictions to FEM computations in 2 cycles loadings. (a): effective constitutive response: $\Sigma_{22} - E_{22}$. (b): porosity evolution $f - E_{22}$

5.2. Relative effect of isotropic and kinematic hardening of the matrix

In this section, we investigate the relative effect of the two types of hardening by showing collective results for $N_r = 10$ cycles. Note here that from now on, only the macroscopic state at the maximum strain U_{max}/L of each cycle will be considered both for the macroscopic uniaxial stress evolution with respect to the number of cycles $\Sigma_{22} - N_r$ and the porosity ratcheting $f - N_r$. More specifically, we first switch off isotropic hardening by setting $N = \infty$ and vary $C/\sigma_0 = 0, 1, 10$. In both Fig.5(a) and 5(b), the MVARX predictions for the macroscopic uniaxial stress response and the porosity evolution are in very good qualitative agreement with the FEM results for this number of cycles. In particular, we observe a slight decrease of the stress with increasing N_r, which is a direct consequence of porosity ratcheting (i.e., porosity increase) as a function of N_r (see Fig.5(b)). In turn, for the porosity evolution, we observe that the MVARX model initially overestimates f but, in turn, the porosity ratcheting slope (i.e., the porosity rate of increase with the number of cycles) is in very good quantitative agreement with the FEM results. Both, the MVARX and the FEM, predict porosity ratcheting, i.e., porosity increase with the number of cycles N_r. Again the initial difference in the porosity prediction at cycle 1 is due to the quadratic character of the MVARX criterion, which tends to overestimate void growth in uniaxial tension loads (as discussed in Fig.3b of Cao et al. (2015)). This can be amended in future studies by use of "cosh" term following a similar procedure with that discussed in Cao et al. (2015) and Mbiakop et al. (2015b).

A second very interesting result, obtained by both the MVARX and the FEM, is that for $C/\sigma_0 = 10$, porosity ratcheting is weaker than for $C/\sigma_0 = 0$ or $C/\sigma_0 = 1$. This implies that significant kinematic hardening could decelerate porosity ratcheting in certain cases. Similar observations were done in the numerical study of Mbiakop et al. (2015a), albeit for a nonlinear kinematic hardening matrix. In Section 6, we carry out a more complete parametric study using the MVARX model to investigate further this effect and we will see that the combined effect between C/σ_0 and N is highly non-trivial and non-monotonic.

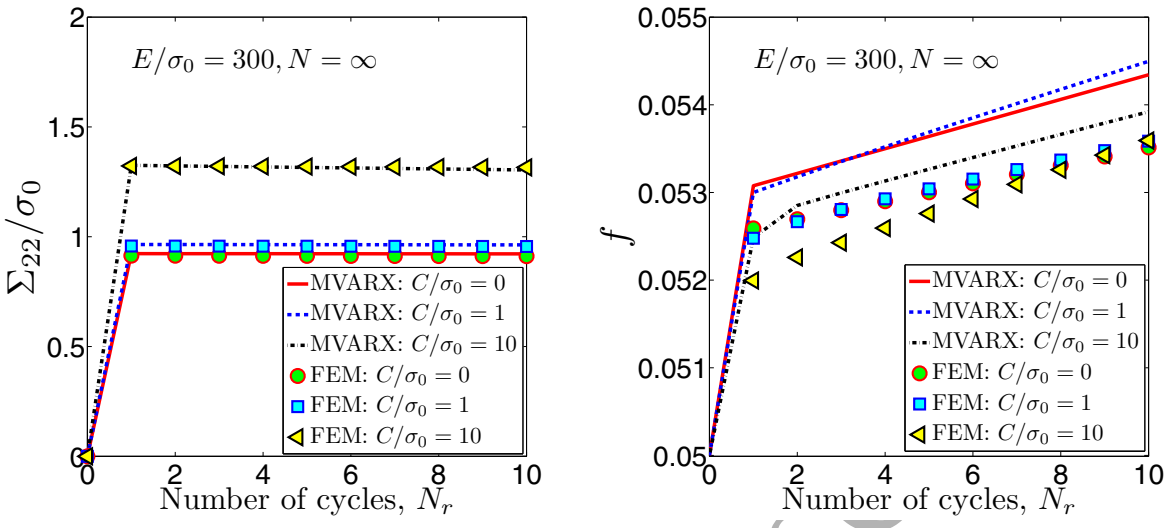

Figure 5: MVARX prediction and validation with FEM computations of the matrix kinematic hardening effect in 10 cycles loadings. (a): effective uniaxial stress variation: $\Sigma_{22} - N_r$. (b): porosity evolution $f - N_r$

Next, in Fig.6, we switch off the kinematic hardening effect by setting $C/\sigma_0 = 0$ and vary $N = \infty, 10$. A striking observation from this figure is that even in the absence of both isotropic and kinematic hardening, i.e, for $N = \infty$ and $C/\sigma_0 = 0$, we observe a significant porosity ratcheting for both the MVARX model and the FEM results. This clearly shows that *elasticity effects are predominant and cannot be neglected*. In fact, it appears that under cyclic loading elasticity is the main mechanism for porosity ratcheting, while hardening seems to slightly affect the porosity ratcheting slopes and its amplitude, in this case. The effect of the matrix elasticity will be specifically studied in section 5.3. Again, the MVARX model is in very good qualitative agreement with the FEM results for both the stress and porosity evolution as a function of the number of cycles. Specifically, in Fig.6(a), the MVARX model is in excellent agreement with the FEM for the prediction of the stress as a function of number of cycles N_r, where we observe a significant increase of the stress due to the isotropic hardening exponent and subsequent saturation at larger number of cycles, as expected. Similar to the previous case discussed, in Fig.6(b), we have porosity ratcheting and, while MVARX overestimates the actual porosity ratcheting (for the same reasons discussed previously in Fig.5), it does on the other hand capture sufficiently well the porosity evolution rate of increase as well as the effect on the hardening exponent N. In fact, in this case, we observe that both MVARX and the FEM give lower porosity ratcheting for $N = 10$ than for $N = \infty$. It should be noted that the present observations are valid for the number of cycles and types of loadings considered and could of course lead to different conclusions if other triaxialities and Lode angles or general loading states are considered (see for instance Mbiakop et al. (2015a)).

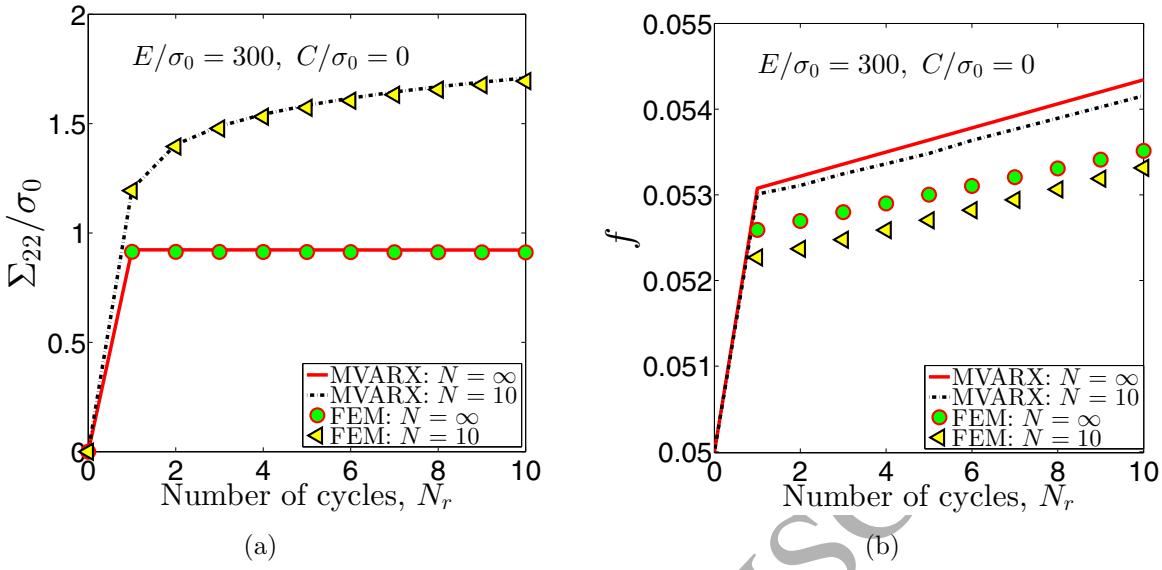

Figure 6: MVARX prediction and validation with FEM computations of the matrix isotropic hardening effect in 10 cycles loadings. (a): effective uniaxial stress variation: $\Sigma_{22} - N_r$. (b): porosity evolution $f - N_r$

5.3. Effect of the matrix elasticity

In this section, we investigate the relative effect of the matrix Young's modulus E upon the stress and porosity evolution as a function of the number of cycles N_r. We thus first consider two values for the Young modulus, $E/\sigma_0 = 300, 1000$ without matrix hardening (i.e. $N = \infty$ and $C/\sigma_0 = 0$). In Fig.7(a), we observe that the stress Σ_{22} is well predicted by the MVARX model when compared with the FEM. The uniaxial yield stresses Σ_{22} (obtained at $U_2 = U_{max}$ of each cycle) is unaffected by the Young's modulus as a consequence of the perfect plasticity considered in this case.

In turn, Fig.7(b) shows an important effect of the matrix elasticity modulus upon porosity ratcheting. As originally discussed by Devaux et al. (1997) (and revisited more recently by Mbiakop et al. (2015a) and Lacroix et al. (2016)), elasticity introduces an asymmetry in the evolution of void growth and shape under a cyclic load. This asymmetry builds up with increasing cycles and leads to different porosity ratcheting responses for different Young's moduli. This effect is relatively well captured by the MVARX model when compared with the FEM results. Specifically, both FEM and MVARX predict an increase of porosity ratcheting with decrease of the Young's modulus.

Additionally, the effect of the matrix elasticity is studied with fixed values of the isotropic hardening exponent $N = 10$ and the linear kinematic hardening constant $C/\sigma_0 = 10$ by adopting three different values of Young modulus $E/\sigma_0 = 300, 1000, 10000$ [5]. It can be

[5]Note that in the previous comparisons illustrated in Figs.7(a) and 7(b) where the matrix hardening is neglected (i.e. $N = \infty$ and $C/\sigma_0 = 0$), corresponding results with $E/\sigma_0 = 10000$ are not shown due to convergence issues appearing in the numerical multi-void unit-cells as a consequence of the perfect plasticity. Nonetheless, similar reduction of porosity ratcheting at very large values of E/σ_0 and perfect plasticity but in a simpler one-void unit-cell have been reported previously in Fig.24 of Mbiakop et al. (2015a).

observed from Fig.7(c) that the stress Σ_{22} is also well predicted by the MVARX model comparing with the FEM computations. The increase of the stress for higher Young's moduli is directly related to the isotropic hardening law used in Eq.(28), where the matrix yield stress is an explicit function of E/σ_0. The corresponding porosity ratcheting is shown in Fig.7(d) and by comparison with the previous results for vanishing matrix hardening (Fig.7(b)), it is evident that elasticity plays a pre-dominant role in porosity ratcheting.

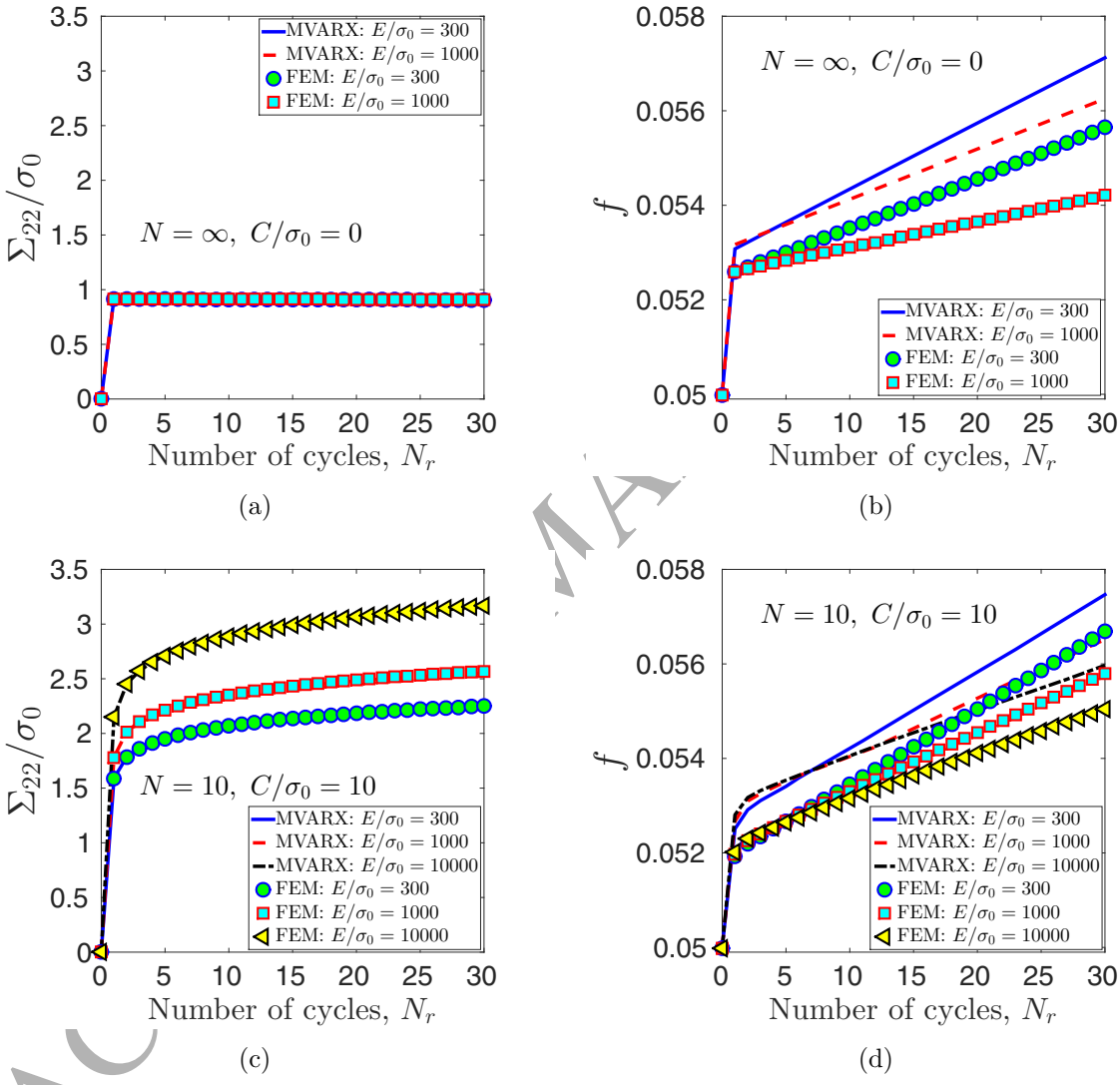

Figure 7: MVARX prediction and validation with FEM computations of the matrix rigidity effect in 30 cycles loadings. (a): effective uniaxial stress variation: $\Sigma_{22} - N_r$. (b): porosity evolution $f - N_r$

In order to understand better the elasticity effect, we show in Fig.8 contours of the axial local plastic strain ε^p_{22} in the cycle $N_r = 30$, at maximum straining U_{max}/L of the porous material with fixed values of the isotropic hardening exponent $N = 10$ and the linear kinematic hardening constant $C/\sigma_0 = 10$. We observe that increase of E/σ_0 leads to more

diffuse plastic zones extending to larger regions in the unit-cell. That is somewhat expected since a high Young's modulus penalizes severely elastic strains and thus the material tends to resort to plasticity. Nonetheless, the plastic strain fields are highly heterogeneous due to the random porous microstructure. In the case of the lowest Young's modulus, $E/\sigma_0 = 300$, plasticity is more localized around the voids and in the inter-void ligaments. This in turn leads to higher void growth and thus larger porosity ratcheting.

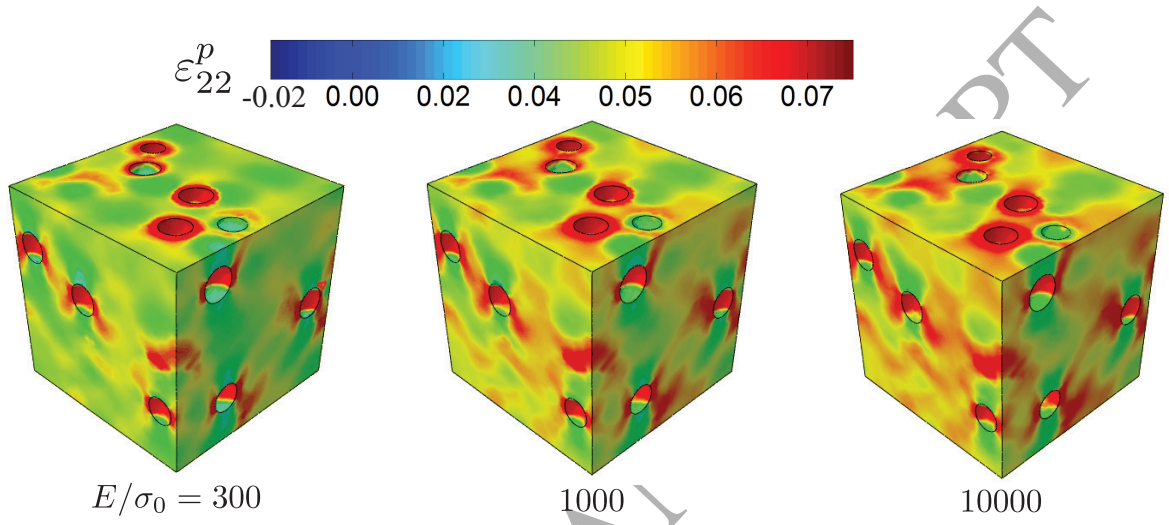

Figure 8: Contours of the axial plastic strain ε^p_{22} in the first generation of mircrostructure (see Fig.2(a)) at the maximum macroscopic strain U_{max}/L of the 30th cycle. Matrix hardening constants: $N = 10$ and $C/\sigma_0 = 10$.

In the following, we illustrate clearly the importance of taking into account the evolution of void volume, shape and orientation during the elastic loading and not only during the plastic loading which is the general practice in porous material modeling since the early work of Gurson. The relevant expressions needed for that has been discussed in detail in section 4.1. Specifically, in Fig.9, we show the stress and porosity evolution as a function of the number of cycles N_r. The stress response in Fig.9(a) shows very slight and negligible dependence upon whether the elastic contribution to the microstructure evolution is taken into account or not. However, porosity ratcheting is strongly affected by elasticity, as clearly observed in Fig.9(b). By neglecting elasticity contribution to the microstructure evolution, porosity ratcheting is significantly weaker and with lower slope. Therefore, in our modeling approach, it appears that this elasticity contribution cannot be neglected, even if the elastic part is reversible. The reason is related to the above described argument of asymmetry in the tension-compression response during the elastic regime which, in fact, has non-negligible effects upon microstructure evolution since the amplitude of elastic strains are comparable to plastic strains in the case of cyclic loading. In fact, the void volume and shape are asymmetrically evolving due to elasticity but also due to isotropic and kinematic hardening.

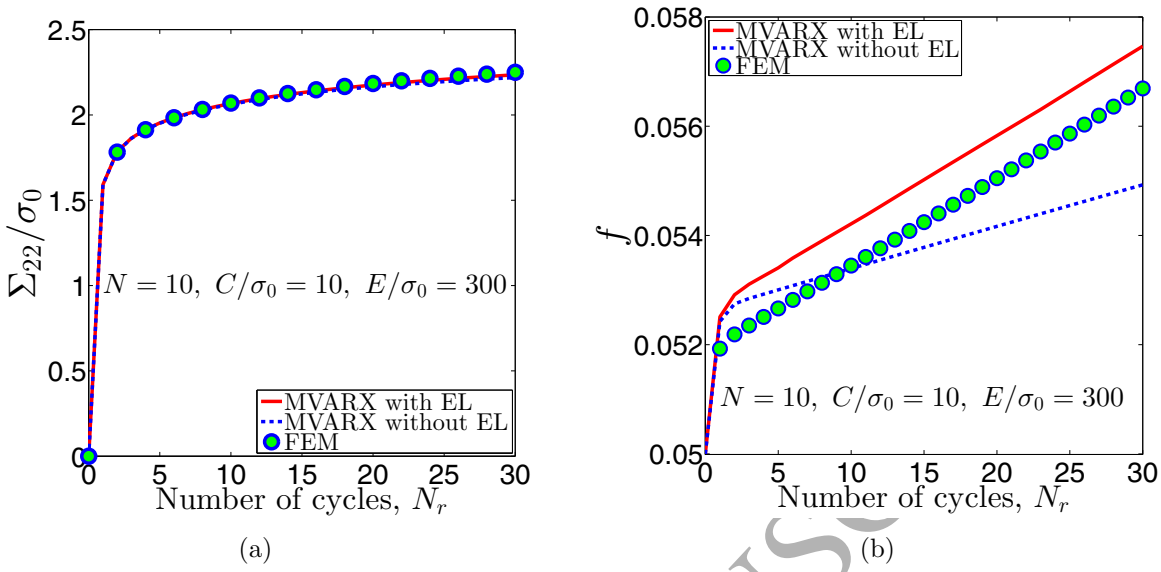

Figure 9: MVARX prediction and validation with FEM computations of the matrix elasticity contribution effect to the microstructure evolution in 30 cycles loadings. (a): effective uniaxial stress variation: $\Sigma_{22} - N_r$. (b): porosity evolution $f - N_r$

5.4. Effect of initial porosity

For completeness, we conclude the assessment of the MVARX model by showing in Fig.10, the effect of initial porosity f_0 on the cyclic response of the porous material. Specifically, in Fig.10(a), the MVARX predicts very accurately the stress response as a function of the number of cycles N_r. By contrast, porosity ratcheting is predicted with much less accuracy as shown in Fig.10(b). Even though, the differences are highly amplified by the normalization of the curves as we show f/f_0 (instead of f where the results look much closer), the present version of the MVARX model tends to overestimate porosity ratcheting at smaller initial porosities such as $f_0 = 0.001$, when compared with the FEM results, even though qualitatively shows the same trends. Thus, the present MVARX estimates should be considered as conservative, while for better accuracy one can either use more accurate homogenization schemes (see for instance Danas and Ponte Castañeda (2009a,b)) or calibrate the model by using more Gurson-type yield surfaces as in Cao et al. (2015). In any case, further calibration of the model with experimental results is necessary for quantitative agreement.

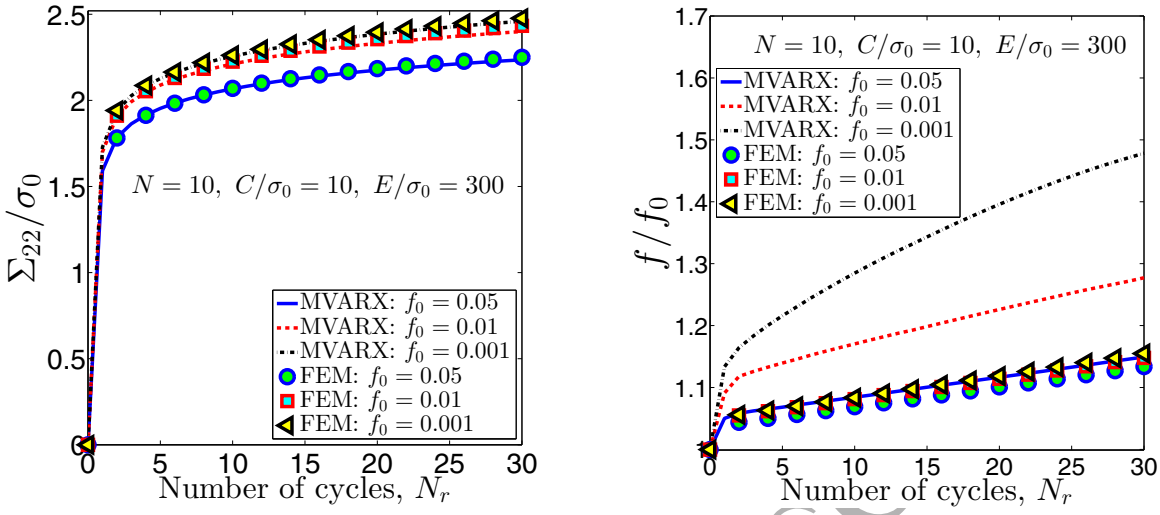

Figure 10: MVARX prediction and validation with FEM computations of the initial porosity effect in 30 cycles loadings. (a): effective uniaxial stress variation: $\Sigma_{22} - N_r$. (b): porosity evolution $f - N_r$

6. MVARX predictions at large number of cycles

In this section, we propose to carry out a parametric study at a larger number of cycles $N_r = 100$ using the MVARX model to understand in more detail the relative effect of isotropic and linear kinematic hardening by varying the isotropic hardening exponent N and the kinematic hardening parameter C/σ_0, for which, as shown in Fig.11, we introduce another two different cyclic loading conditions. In this figure, in addition to the usual tension-compression with zero average cyclic load (Fig.11(a)), we also consider cyclic loads with tension loading-elastic unloading with a non-zero positive mean stress (Fig.11(b)), as well as with a positive prestress and cycling this point (Fig.11(c)). Again, we control the axial displacement U_2 (or the average strain $E_{22} = U_2/L$), such that the average nominal strain takes the value $E_{22} = 0.05$. This allows to enter well the plastic region, while the elastic strains remaining still significant. For the sake of brevity of this parametric study, we keep the rest of the parameters fixed, i.e., the Young's modulus $E/\sigma_0 = 300$, Poisson ratio $\nu = 0.3$, initial porosity $f = 5\%$, and initially spherical void shapes.

- Type 1 (see Fig.11(a)): Same loading condition as discussed in Section 5.
- Type 2 (see Fig.11(b)): In each cycles, U_2 initially increases from $U_2 = 0$ to $U_2 = U_{max}$ (note that $U_{max}/L = 0.05$), then unloads from $U_2 = U_{max}$ to $U_2 = 0$.
- Type 3 (see Fig.11(c)): U_2 initially increases from $U_2 = 0$ to $U_2 = U_{max}$, then unloads - loads between $U_2 = U_{max}$ to $U_2 = U_{max}/2$.

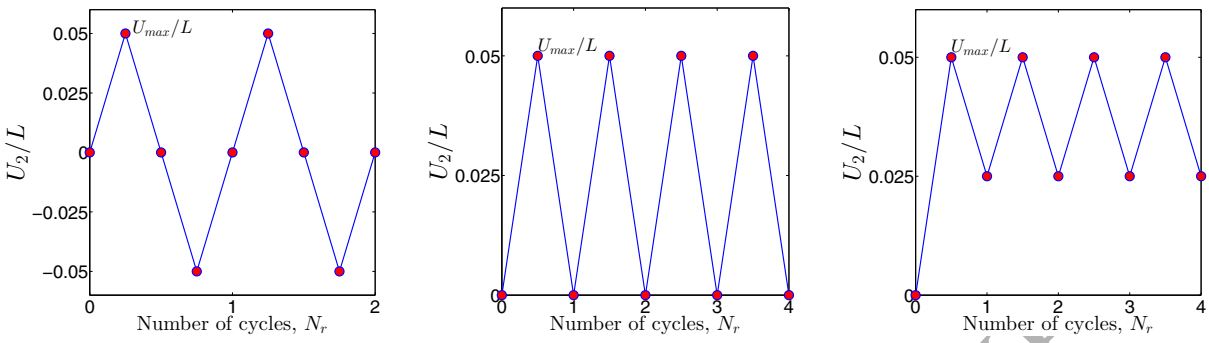

(a) Type 1 (b) Type 2 (c) Type 3

Figure 11: Schematic explanation of three types of uniaxial cyclic loading

In Fig.12, we investigate the effect of cyclic loading type on porosity ratcheting for various values of N and C/σ_0. First of all, in the absence of any hardening, the MVARX model predicts porosity ratcheting, as shown in 12(a), which is in agreement with the corresponding FEM results in Fig.6(b). This is true for all loading Types 1, 2 and 3 considered in this study. In addition, by comparing Figs.12(a)- 12(b) and Figs.12(c)- 12(d), we note that the addition of kinematic hardening introduces a weak initial decrease of f for loading Types 1 and 2 at small number of cycles, while its effect smears out at larger number of cycles. It can also observed by comparing Fig.12(a) and 12(b) that the addition of linear kinematic hardening tends to decelerate the porosity ratcheting when $N = \infty$.

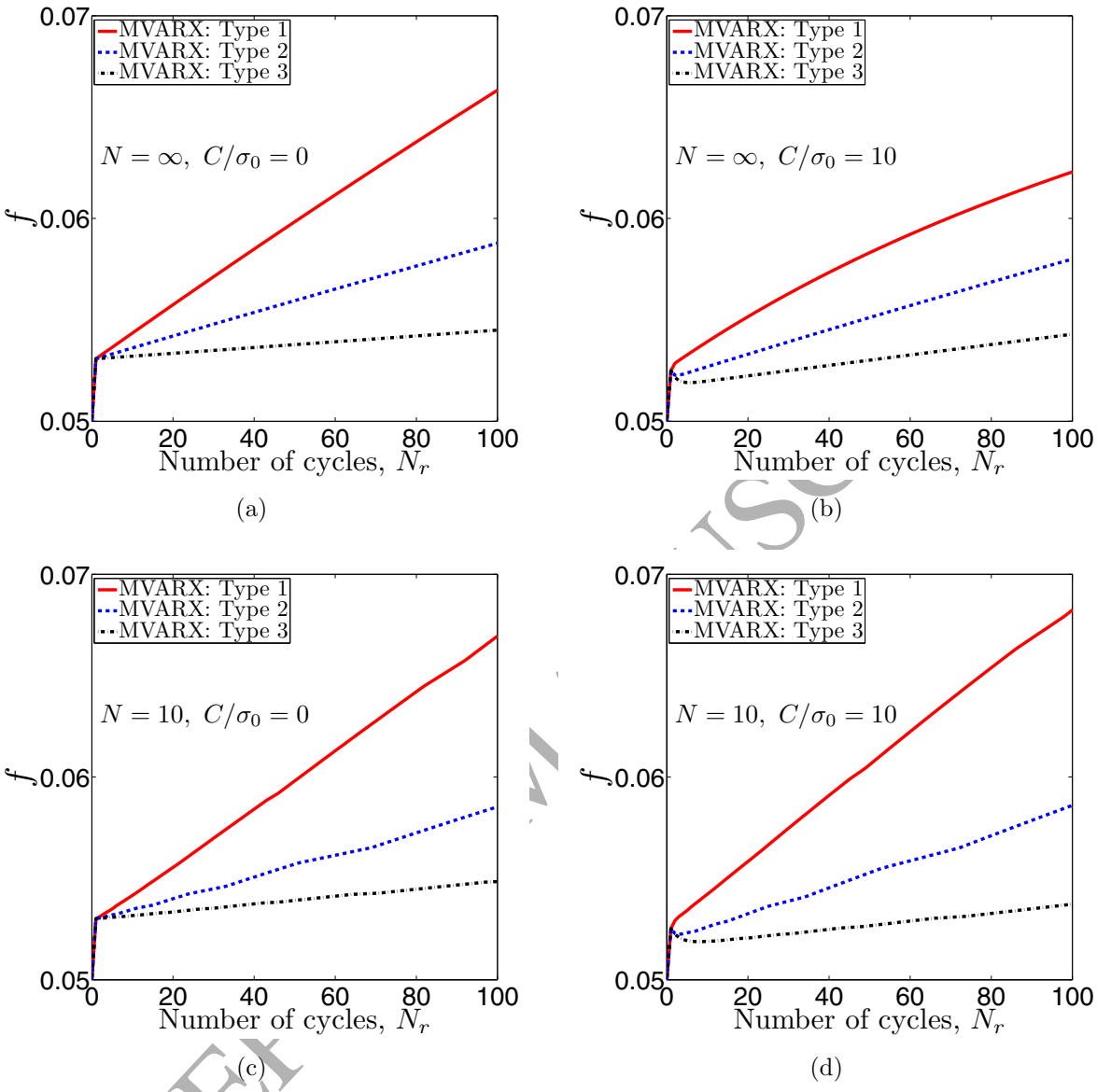

Figure 12: Effect of cyclic loading type on porosity ratcheting for various values of N and C/σ_0.

6.1. Relative effect of hardening for the three loading types

Fig.13 shows the porosity evolution curves for $N = \infty, 10, 5$ for three different kinematic hardening modulus of $C/\sigma_0 = 0, 1, 10$ in the case of the loading type 1 as defined in Fig.11(a). From these curves, it is evident that the interplay between the isotropic and kinematic hardening is non-trivial. For instance, depending on the exponent N, the addition of kinematic hardening can either reduce (see for instance $N = \infty$ in Fig.13(a)) or increase (see for instance $N = 5$ in Fig.13(c)) porosity ratcheting for this type of loading.

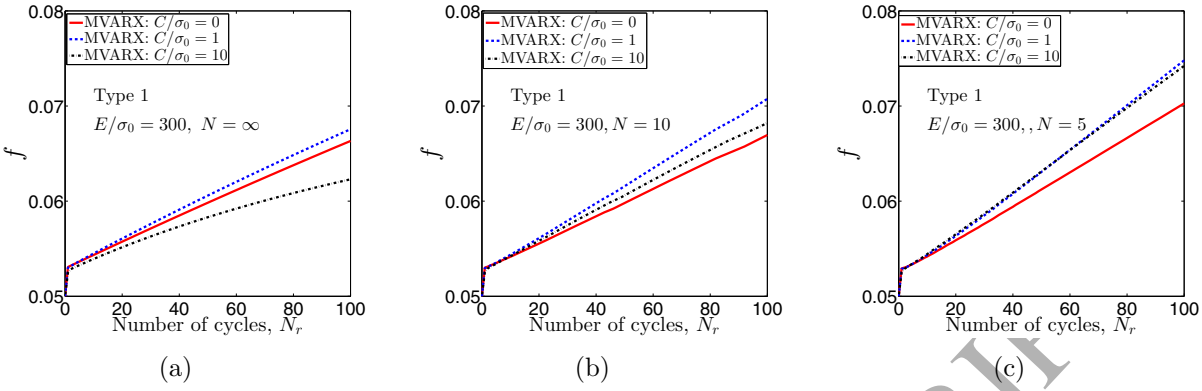

Figure 13: Detail porosity evolution within 100 cycles of the Type 1 cyclic loading with several matrix hardening parameters (a): without matrix isotropic hardening $N = \infty$ and $C/\sigma_0 = 0$, 1, 10 , (b): $N = 10$ and $C/\sigma_0 = 0$, 1, 10, (c): $N = 5$ and $C/\sigma_0 = 0$, 1, 10

For a more comprehensive visualization, we show in Fig.14 the cross plots of porosity at $U_2 = U_{max}$ of $N_r = 100$ cycles. Specifically, in Fig.14(a), we observe that decrease of N (or equivalently increase of $1/N$) could lead to a non-monotonic effect for f if $C/\sigma_0 = 0$ while it remains monotonically increasing if $C/\sigma_0 = 10$. In turn, in Fig.14(b), decrease of N from ∞ to 5 leads to a general increase in porosity ratcheting. Again the relative effect of C/σ_0 is non-monotonic with the maximum observed at $C/\sigma_0 \sim 1$. Beyond that point, kinematic hardening tends to decelerate porosity ratcheting for all N considered here.

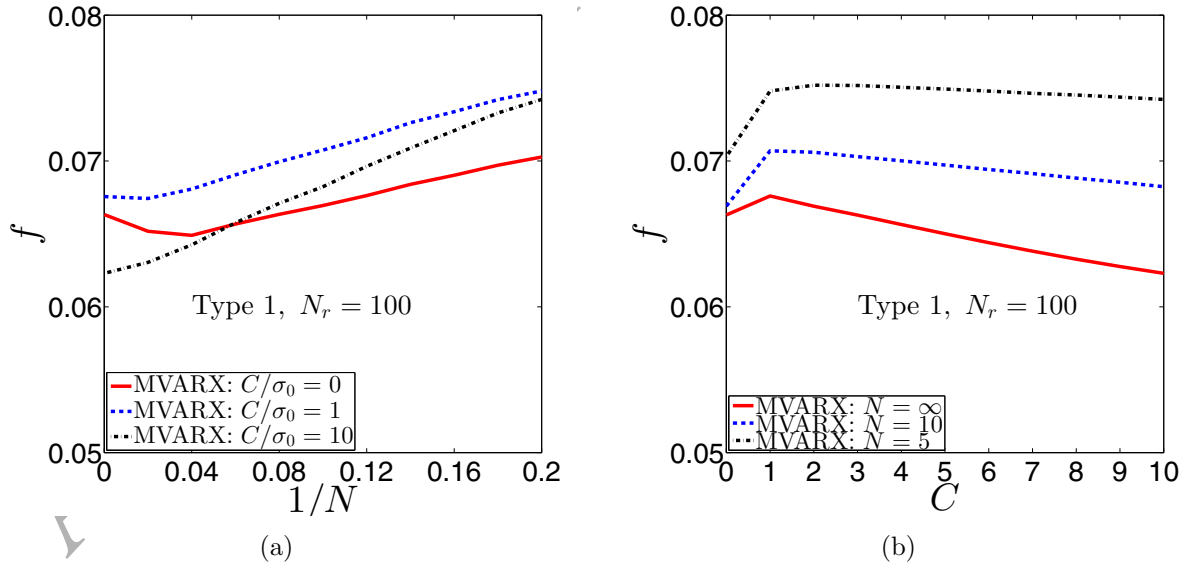

Figure 14: MVARX predictions of porosity at 100 cycles for Type 1 cyclic loading with symmetric tension/compression loads. (a): C/σ_0 is respectively fixed at 0, 1, 10 and N varies between ∞ and 5 (i.e. $1/N$ varies between 0 and 0.2) (b): N is respectively fixed at ∞, 10, 5 and C/σ_0 varies between 0 and 10.

Next, Fig.15, shows porosity evolution curves for $N = \infty, 10, 5$ for three different kine-

matic hardening values of $C/\sigma_0 = 0, 1, 10$ in the case of the loading type 2 as defined in Fig.11(b), which corresponds to a tension loading and elastic unloading with no overall compression. In this case, observe a relatively minor effect of both the kinematic hardening parameter C/σ_0 and the isotropic hardening exponent N. Moreover, for all N, we observe a crossover of the curves. Again for a better illustration, Fig.16 shows cross plots of porosity at $N_r = 100$ cycles. Even though, in Fig.16(a), we observe a minimum of f for $1/N \sim 0.02$, the curves seem to be rather insensitive to both N and C/σ_0.

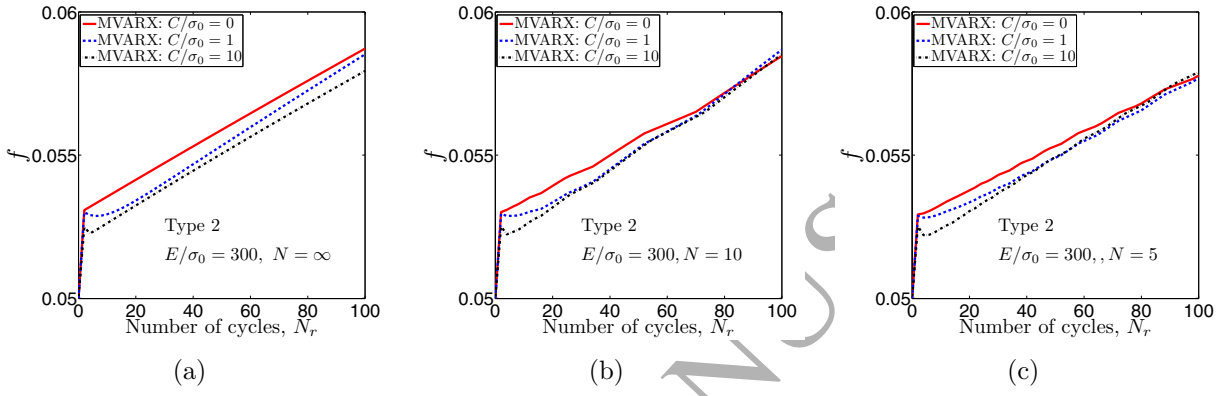

Figure 15: Detail porosity evolution within 100 cycles of the Type 2 cyclic loading with several matrix hardening parameters (a): without matrix isotropic hardening $N = \infty$ and $C/\sigma_0 = 0$, 1, 10 , (b): $N = 10$ and $C/\sigma_0 = 0$, 1, 10, (c): $N = 5$ and $C/\sigma_0 = 0$, 1, 10

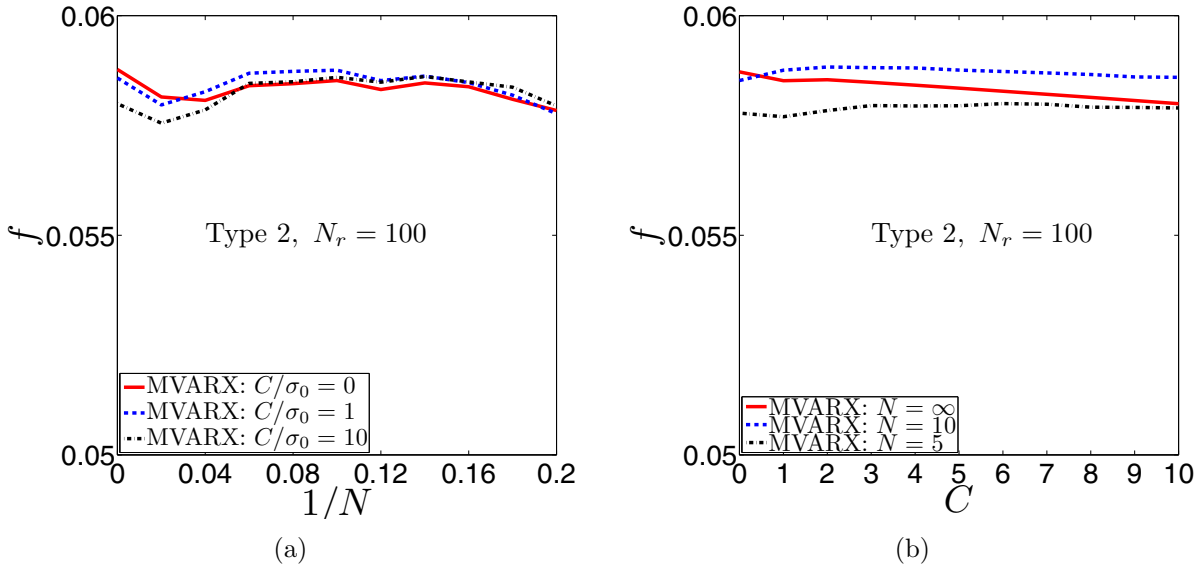

Figure 16: MVARX predictions of porosity at 100 cycles for Type 2 cyclic loading. (a): C is respectively fixed at 0, 1, 10 and N varies between ∞ and 5 (i.e. $1/N$ varies between 0 and 0.2 (b): N is respectively fixed at ∞, 10, 5 and C/σ_0 varies between 0 and 10.

Fig.17, shows porosity evolution curves for $N = \infty, 10, 5$ for three different kinematic hardening values of $C/\sigma_0 = 0, 1, 10$ for the loading type 3 defined in Fig.11(b), which corresponds to a positive tensile pre-stress and subsequent cyclic loading around this pre-stress. In this case, we observe a significant cross-over of the curves for $N = \infty$ but no cross-over for $N = 5$ for increasing number of cycles N_r. For instance, when $N = \infty$, the porosity curve corresponding to $C/\sigma_0 = 10$ initially decreases with N_r attaining a minimum at $N_r \sim 5$ and then starts increasing again as N_r goes to 100 cycles. Similar to the previous cases, Fig.18 shows corresponding cross-plots of porosity at $N_r = 100$ cycles. In this case, in Fig.18(b), f decreases to an asymptote as C/σ_0 increases except for $N = \infty$ that exhibits first a minimum. In turn, Fig.18(a) shows a highly non-monotonic response of f, exhibiting a maximum for $1/N \sim 0.04$ (or $N \sim 25$). In this type of loading, increase of $1/N$, i.e., a material with significant isotropic hardening tends to reduce porosity ratcheting .

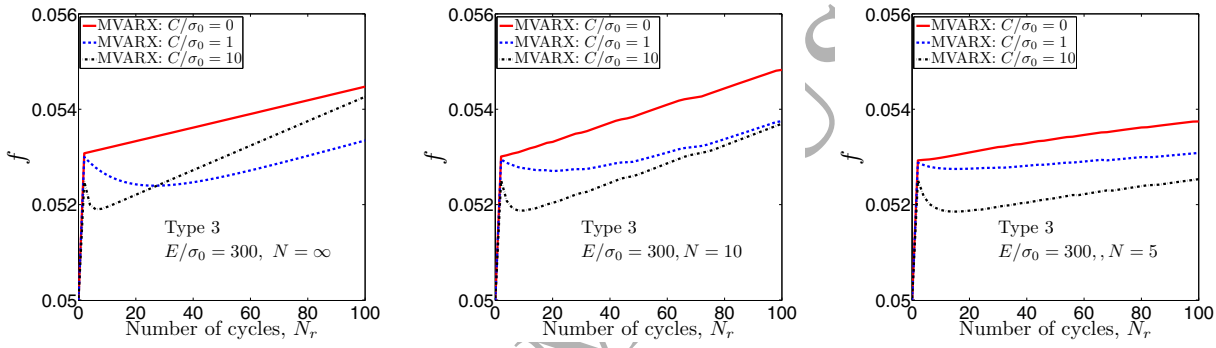

(a) (b) (c)

Figure 17: Detail porosity evolution within 100 cycles of the Type 3 cyclic loading with several matrix hardening parameters (a): without matrix isotropic hardening $N = \infty$ and $C/\sigma_0 = 0$, 1, 10 , (b): $N = 10$ and $C/\sigma_0 = 0$, 1, 10, (c): $N = 5$ and $C/\sigma_0 = 0$, 1, 10

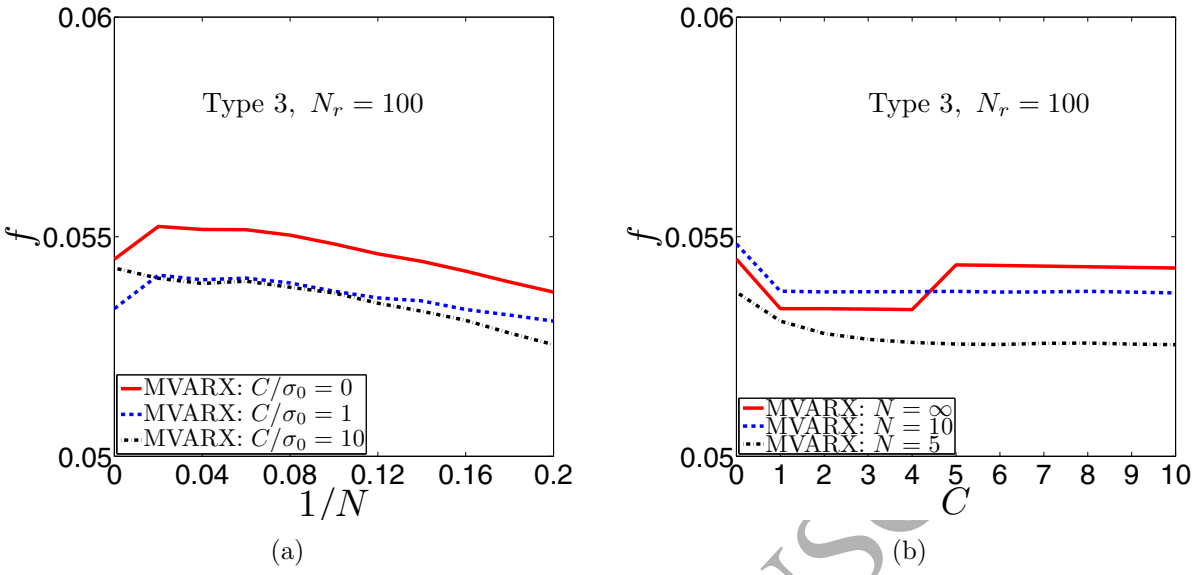

Figure 18: MVARX prediction of the matrix hardening effect on the porosity evolution at 200 cycles of Type 3 cyclic loading. (a): C is respectively fixed at 0, 1, 10 and N varies between ∞ and 5 (i.e. $1/N$ varies between 0 and 0.2 (b): N is respectively fixed at ∞, 10, 5 and C/σ_0 varies between 0 and 10.

7. Concluding remarks

In this work, we have developed a nonlinear homogenization model (termed MVARX) to study the response of elasto-plastic porous material with an isotropic and linear kinematic hardenable matrix subjected to cyclic loading and finite strains. The proposed model is an extension of the MVAR model of Danas and Aravas (2012) to include linear kinematic hardening and evolution of microstructure during elastic loading. It is obtained by use of a decoupled homogenization strategy and is used to describe both the elastic and plastic effective response. The resulting effective back stress in the homogenized model, as for the macroscopic stress and plastic strain, has non-zero hydrostatic terms as a result of the homogenization procedure for a porous material. The model is also numerically implemented in an efficient general purpose user-material subroutine for structural calculations. The model is extensively validated by full field finite element calculations of multi-void periodic unit cells for a number of hardening and elastic parameters. A major finding of this work is that elasticity is the predominant mechanism for porosity ratcheting as illustrated by both the numerical analysis and the analytical model.

Specifically, the MVARX model is found to be in very good qualitative agreement with the finite element results for all loading types, hardening parameters and porosities considered. Specifically, porosity ratcheting is predicted by both the numerical analysis and the analytical model and is found to be a non-trivial consequence of both the isotropic and linear kinematic hardening. The effect of linear kinematic hardening is shown to be weaker than that of the isotropic hardening at large number of cycles but still present. The main reason for the observed porosity ratcheting is the initial asymmetry introduced in the response of

the porous solid during the first cycles, which lead to an asymmetric evolution of the microstructure during tension and compression. This asymmetry builds up with the increase of the cycles. This explains partially the importance of the isotropic hardening in porosity ratcheting, which is predominant in the first cycles and then as is well-known saturates at larger cycles.

A second observation, which was found to be of critical importance in our modeling approach, is the effect of elasticity in the evolution of microstructure. Elastic effects combined of course with hardening effects contribute even more to the asymmetric evolution of the porosity and need to be taken into account in the analytical modeling approach. Since our modeling uses standard linear homogenization techniques for the linear regime, such an operation is straightforward by direct use of the phase concentration (or localization) tensors, which are readily available from the homogenization procedure. The plastic part of the homogenization is built along the lines discussed by Aravas and Ponte Castañeda (2004) and more recently by Danas and Aravas (2012).

The MVARX model was used then to investigate three different cyclic loading types and effects of several values of the isotropic and linear kinematic hardening parameters. The three loading types considered involve a standard tension/compression cycle with equal amplitude positive and negative axial strain, a tension loading-elastic unloading with a non-zero positive average stress state, as well as a cyclic load where a positive prestress is added first and then cycling around this point is carried out. For the amplitudes considered here, the tension/compression load is found to lead to the largest porosity ratcheting effect while the positive prestress load to the smallest one. The relative effect of isotropic and kinematic hardening in those three loading states is found to be very different. In the last two loading types the kinematic hardening appears to have a weaker effect than in the first one. The effect of the corresponding isotropic hardening on the porosity ratcheting is most of the times non-monotonic and therefore highly non-trivial.

We conclude this work by noting that the present model was found to be less accurate in quantitative terms especially at smaller initial porosities. This is mainly attributed to the quadratic character of the original MVAR model of Danas and Aravas (2012) and carries on to the present MVARX model, which tends to overestimate the porosity evolution in the first cycle for uniaxial tension loads. To amend this, Cao et al. (2015) has proposed a modification of the original MVAR model for monotonic loads, which consists in re-writing it in a Gurson-type form. This led to a decrease of the porosity estimation and a better agreement with corresponding finite element results. Such a modification is straightforward in the present model since it affects only the plastic part and will be pursued in a future study. Again, as shown in Cao et al. (2015), the present model could be easily calibrated by use of a very small number of parameters in order to describe experimental data.

Last but not least, the proposed model is able to deal with general initial void shapes and orientations but such a study has not been attempted here for the sake of keeping the work focused and concise. However, as has been discussed by Mbiakop et al. (2015a), the initial void shape as well as different triaxialities have significant effects on the cyclic response of the porous solids. Such a study is left for the future. Alternatively, the consideration of a fully coupled homogenization method (Lahellec and Suquet, 2007; Idiart and Lahellec, 2016)

may also constitute a challenging extension at finite strains, which could pave the way to a refined, probably more quantitative porosity ratcheting prediction.

Acknowledgement

This work was funded by the French National Research Agency through the ANR project INDIANA (grant ANR-12-RMNP-0011). K.D. would also like to acknowledge partial support from the European Research Council (ERC) under the European Union's Horizon 2020 research and innovation program (Grant Agreement No. 636903).

Appendix A. Numerical implementation of the MVARX model

This section describes the numerical implementation of the aforementioned constitutive model. First, it is essential to define the velocity boundary conditions that are related to the applied finite strains. Thus, one has

$$\boldsymbol{v} = \boldsymbol{\mathcal{L}} \cdot \boldsymbol{x}, \quad \text{with} \quad \boldsymbol{\mathcal{L}} = \dot{\boldsymbol{F}} \cdot \boldsymbol{F}^{-1} \tag{A.1}$$

where $\boldsymbol{\mathcal{L}}$ and $\boldsymbol{F}$ are respectively the macroscopic velocity gradient and macroscopic deformation gradient. The symmetric and skew-symmetric part of $\boldsymbol{\mathcal{L}}$ denote the macroscopic strain-rate $\boldsymbol{D} = 1/2\left[\boldsymbol{\mathcal{L}} + \boldsymbol{\mathcal{L}}^T\right]$ and the macroscopic spin $\boldsymbol{W} = 1/2\left[\boldsymbol{\mathcal{L}} - \boldsymbol{\mathcal{L}}^T\right]$. Note that similar to the decomposition of the strain-rate to an elastic part and a plastic part (see equation (30)), we also decompose the macroscopic spin tensor to $\boldsymbol{W} = \boldsymbol{W}_e + \boldsymbol{W}_p$. Those tensors have already been used in the previous sections to describe the evolution of the void orientation vectors in the elastic and plastic regime.

Remark: For non-viscous plasticity, the magnitude of $\boldsymbol{v}$ (or $\boldsymbol{\mathcal{L}}$) does not affect the final result. Hence, the total displacement $\boldsymbol{u}$ is expressed in terms of the velocity $\boldsymbol{v}$ via $\boldsymbol{u} = \boldsymbol{x} - \boldsymbol{\zeta} = \boldsymbol{v} \cdot t$ $(t_n \leq t \leq t_{n+1})$, where $\boldsymbol{x}$ and $\boldsymbol{\zeta}$ respectively define the deformed current configuration and the undeformed reference configuration. while $\boldsymbol{v}$ is constant in time t.

Moreover, in order to implement the present model, we recall here the polar decomposition of the deformation gradient $\boldsymbol{F}(t)$ into a rotation tensor $\boldsymbol{R}(t)$ and right stretch tensor $\boldsymbol{U}(t)$ during the time increment $[t_n, t_{n+1}]$, such that

$$\boldsymbol{F}(t) = \triangle\boldsymbol{F}(t) \cdot \boldsymbol{F}_n = \boldsymbol{R}(t) \cdot \boldsymbol{U}(t) \cdot \boldsymbol{F}_n, \qquad \boldsymbol{R}^T(t) \cdot \boldsymbol{R}(t) = \boldsymbol{I} \tag{A.2}$$

The strain-rate and the spin tensors can then be obtained from (A.1) as

$$\begin{aligned} \boldsymbol{D}(t) =& \frac{1}{2}\left[(\triangle\dot{\boldsymbol{F}}(t) \cdot \triangle\boldsymbol{F}(t)) + (\triangle\dot{\boldsymbol{F}}(t) \cdot \triangle\boldsymbol{F}(t))^T\right], \\ \boldsymbol{W}(t) =& \frac{1}{2}\left[(\triangle\dot{\boldsymbol{F}}(t) \cdot \triangle\boldsymbol{F}(t)) - (\triangle\dot{\boldsymbol{F}}(t) \cdot \triangle\boldsymbol{F}(t))^T\right]. \end{aligned} \tag{A.3}$$

Furthermore, using the logarithmic strain $\boldsymbol{E}(t) = \ln \boldsymbol{U}(t)$ at the beginning of the time increment $t = t_n$ and assuming that the eigenvectors of $\boldsymbol{U}(t)$ remain constant in the time increment $[t_n, t_{n+1}]$, one has

$$\boldsymbol{D}(t) = \boldsymbol{R}(t) \cdot \dot{\boldsymbol{E}}(t) \cdot \boldsymbol{R}^T(t), \qquad \boldsymbol{W}(t) = \dot{\boldsymbol{R}}(t) \cdot \boldsymbol{R}^T(t) \tag{A.4}$$

Using this last decomposition, one can write the Jaumann rates of the macroscopic stress, the macroscopic backstres, and the orientation vectors as

$$\overset{\triangledown}{\boldsymbol{\Sigma}}(t) = \boldsymbol{R}(t) \cdot \dot{\widehat{\boldsymbol{\Sigma}}}(t) \cdot \boldsymbol{R}^T(t), \quad \overset{\triangledown}{\boldsymbol{X}}(t) = \boldsymbol{R}(t) \cdot \dot{\widehat{\boldsymbol{X}}}(t) \cdot \boldsymbol{R}^T(t),, \quad \overset{\triangledown}{\boldsymbol{n}}^{(i)}(t) = \boldsymbol{R}(t) \cdot \dot{\widehat{\boldsymbol{n}}}^{(i)}(t) \quad \text{(A.5)}$$

where the quantities with the superscript $\widehat{(\,)}$ are the usual time derivatives.

To be more precise, one has at each Gauss integration point the following known and unknown quantities:

- at the beginning of the increment $t = t_n$, the known quantities are:

$$\boldsymbol{F}_n, \quad \boldsymbol{F}_{n+1}, \quad \boldsymbol{\Sigma}_n, \quad \boldsymbol{X}_n, \quad \boldsymbol{s}_\alpha \mid_n \tag{A.6}$$

- at the end of the increment $t = t_n + 1$, the following quantities need to be computed

$$\boldsymbol{\Sigma}_{n+1}, \quad \boldsymbol{X}_{n+1}, \quad \boldsymbol{s}_\alpha \mid_{n+1}. \tag{A.7}$$

Next, in order to probe the plastic yield surface, we introduce the standard "elastic predictor" as

$$\widehat{\boldsymbol{\Sigma}}^e = \widehat{\boldsymbol{\Sigma}}_n + \widetilde{\mathbb{L}}_e : \triangle \boldsymbol{E}. \tag{A.8}$$

As is usual in elasto-plastic integration schemes, if $\widetilde{\Phi}(\widehat{\boldsymbol{\Sigma}}^e - \widehat{\boldsymbol{X}}_n, \widehat{\boldsymbol{s}}_\alpha \mid_n) < 0$, the material is elastically loaded and the linear elastic equations have to be used, whereas if $\widetilde{\Phi} \geq 0$ the material is plastically loaded.

Appendix A.1. Elasticity implementation

In the case of $\widetilde{\Phi} < 0$, the porous material is under elastic loading thus is convenient to adopt the forward Euler method to compute the unknowns listed above (A.7), which leads to

$$\begin{aligned}
&\widehat{\boldsymbol{\Sigma}}_{n+1} = \widehat{\boldsymbol{\Sigma}}^e \\
&\widehat{\boldsymbol{X}}_{n+1} = \widehat{\boldsymbol{X}}_n \\
&f_e \mid_{n+1} = f_e \mid_n \, \exp\left[\mathrm{tr}(\mathbb{A}_e^{(2)} \mid_n : \triangle \boldsymbol{E}) - \mathrm{tr}(\triangle \boldsymbol{E})\right] \\
&(w_e)_1 \mid_{n+1} = (w_e)_1 \mid_n + (w_e)_1 \mid_n \, (\boldsymbol{n}^{(3)} \otimes \boldsymbol{n}^{(3)} - \boldsymbol{n}^{(1)} \otimes \boldsymbol{n}^{(1)}) : \mathbb{A}_e^{(2)} \mid_n : \triangle \boldsymbol{E} \\
&(w_e)_2 \mid_{n+1} = (w_e)_2 \mid_n + (w_e)_2 \mid_n \, (\boldsymbol{n}^{(3)} \otimes \boldsymbol{n}^{(3)} - \boldsymbol{n}^{(2)} \otimes \boldsymbol{n}^{(2)}) : \mathbb{A}_e^{(2)} \mid_n : \triangle \boldsymbol{E} \\
&\widehat{\boldsymbol{n}}_e^{(i)} \mid_{n+1} = \exp\left(-\boldsymbol{W}_e^E \mid_n\right) \widehat{\boldsymbol{n}}_e^{(i)} \mid_n
\end{aligned} \tag{A.9}$$

It should be noted that the porosity at the end of the time increment $f_e \mid_{n+1}$ can be directly evaluated from equation (37).

Appendix A.2. Plasticity implementation

If $\widetilde{\Phi} \geq 0$, the porous material is under plastic loading. In this case, the elastic predictor $\boldsymbol{\Sigma}^e$ is corrected to satisfy the plastic criterion (29) through

$$\widehat{\boldsymbol{\Sigma}}_{n+1} = \widehat{\boldsymbol{\Sigma}}^e - \widetilde{\mathbb{L}}_e \mid_n : \triangle \boldsymbol{E}^p + \triangle\Lambda(\widehat{\boldsymbol{\Sigma}}_n \cdot \boldsymbol{\Omega}_n^p - \boldsymbol{\Omega}_n^p \cdot \widehat{\boldsymbol{\Sigma}}_n) \tag{A.10}$$

Due to the linear kinematic hardening obtained in the present model and the Jaumann rate definition in $(51)_2$, the macroscopic back stress $\widehat{\boldsymbol{X}}_{n+1}$ at the end of the time increment $t = t_{n+1}$ takes the form

$$\widehat{\boldsymbol{X}}_{n+1} = \widehat{\boldsymbol{X}}_n + \widetilde{\mathbb{L}}_X \mid_n : \triangle \boldsymbol{E}^p + \triangle\Lambda(\widehat{\boldsymbol{X}}_n \cdot \boldsymbol{\Omega}_n^P - \boldsymbol{\Omega}_n^P \cdot \widehat{\boldsymbol{X}}_n). \tag{A.11}$$

Next, the accumulated plastic strain at the end of time increment is calculated via

$$\bar{\varepsilon}^p_{n+1} = \bar{\varepsilon}^p_n + \frac{\widehat{\boldsymbol{\Sigma}}_n : \triangle \boldsymbol{E}}{(1 - f_n)\sigma_0(\bar{\varepsilon}^p_n)} \tag{A.12}$$

Following the combined implicit-explicit scheme of Aravas and Ponte Castañeda (2004) and Danas and Aravas (2012), the microstructure variables at $t = t_{n+1}$ can be computed by

$$\begin{aligned}
&f_p \mid_{n+1} = f_p \mid_n + \alpha_f \, (1 - f_p \mid_n) \mathrm{tr}(\triangle \boldsymbol{E}) \\
&(w_p)_1 \mid_{n+1} = (w_p)_1 \mid_n + \alpha_w \, (w_p)_1 \mid_n (\boldsymbol{n}^{(3)} \otimes \boldsymbol{n}^{(3)} - \boldsymbol{n}^{(1)} \otimes \boldsymbol{n}^{(1)}) : \mathbb{A}_p^{(2)} \mid_n : \triangle \boldsymbol{E} \\
&(w_p)_2 \mid_{n+1} = (w_p)_2 \mid_n + \alpha_w \, (w_p)_2 \mid_n (\boldsymbol{n}^{(3)} \otimes \boldsymbol{n}^{(3)} - \boldsymbol{n}^{(2)} \otimes \boldsymbol{n}^{(2)}) : \mathbb{A}_p^{(2)} \mid_n : \triangle \boldsymbol{E} \\
&\widehat{\boldsymbol{n}}_p^{(i)} \mid_{n+1} = \exp\left(-\triangle\Lambda \boldsymbol{\Omega}_n^P\right) \cdot \widehat{\boldsymbol{n}}_p^{(i)} \mid_n
\end{aligned} \tag{A.13}$$

Equations (A.13) provide an explicit scheme for the microstructural variables during plastic loading phase. Note that the stability of this numerical approach is very good by using below a fully implicit scheme for the plastic strains and yield function. In fact such a scheme was found to work better than a fully implicit scheme for all variables of the problem.. In this regard then, the above equations (A.13), $\triangle\Lambda$ and $\triangle \boldsymbol{E}$ are evaluated using a standard Newton-Raphson scheme in the instantaneous yield function and plastic flow equations

$$\begin{aligned}
\widetilde{\Phi}(\widehat{\boldsymbol{\Sigma}}_{n+1} - \widehat{\boldsymbol{X}}_{n+1}, \widehat{\boldsymbol{s}}_\alpha \mid_n) = 0 \qquad &(\#1) \\
\triangle \boldsymbol{E}^p = \triangle\Lambda \, \widehat{\boldsymbol{N}}_{n+1} \qquad &(\#6).
\end{aligned} \tag{A.14}$$

Here the symbol # is used to denote the number of equations. Note also that for simplicity in the present work we use the continuum tangent elastoplastic modulus (60) described in Section 4.3.

References

Aravas, N., 1987. On the numerical integration of a class of pressuredependent plasticity models. Int. J. Numer. Meth. Engin., 24, 7, 1395–1416.

Aravas, N., Ponte Castañeda, P, 2004. Numerical methods for porous metals with deformation-induced anisotropy. Computer methods in applied mechanics and engineering, 193, 3767-3805.

Armstrong, P. J., Frederick, C. O., 1966. A mathematical representation of the multiaxial baushinger effect, Note RD/B/N731, Berkeley Nuclear Laboratories.

Besson. J., Guillemer-Neel,C., 2003. An extension of the Green and Gurson models to kinematic hardening. Mechanics of materials, 25, 1-18.

L. Brassart, L. Stainier, I. Doghri, L. Delannay, 2011. A variational formulation for the incremental homogenization of elasto-plastic composites. Journal of the Mechanics and Physics of Solids, 59 (12), Pages 2455–2475.

Brocks, W., Steglich, D., 2003. Damage models for cyclic plasticity. Key Engineering Materials 251-252, 389–398.

Cao, T. S., Mazière, M., Danas, K., Besson, J., 2015. A model for ductile damage prediction at low stress triaxialities incorporating void shape change and void rotation. International Journal of Solids and Structures, 63, 240-263.

Chaboche, J. L., Jung, O., 1998. Application of a kinematic hardening viscoplasticity model with thresholds to the residual stress relaxation. International Journal of Plasticity, 13, No.10, 785-807.

Chaboche, J. L., 2008. A review of some plasticity and viscoplasticity constitutive theories. International Journal of Plasticity, 24, 1642-1693.

E. Charkaluk, A. Constantinescu, F. Szmytka, S. Tabibian, 2014. Probability density functions: From porosities to fatigue lifetime. International Journal of Fatigue 63, 127–136

Dafalias, Y., F., 1985. The plastic spin. J. Appl. Mech. 52, 865–871.

N. Dahdah, N. Limodin, A. El Bartali, J. F. Witz, R. Seghir, E. Charkaluk, J. Y. Buffiere, 2016. Damage Investigation in A319 Aluminium Alloy by Xray Tomography and Digital Volume Correlation during In Situ High-Temperature Fatigue Tests. Strain 52, 324–335.

Danas, K., Aravas, N., 2012. Numerical modeling of elasto-plastic porous materials with void shape effects at finite deformations. Composites: Part B, 43(6), 2544-2559.

Danas K., Ponte Castañeda P. 2009a. A finite-strain model for viscoplastic anisotropic porous media: I-Theory, Eur. J. Mechanics A/Solids, 28, 387-401.

Danas K., Ponte Castañeda P. 2009b. A finite-strain model for viscoplastic anisotropic porous media: II-Applications, Eur. J. Mechanics A/Solids, 28, 402-416

Sebastien Dezecot, Jean-Yves Buffiere, Alain Koster, Vincent Maurel, Fabien Szmytka, Eric Charkaluk, Nora Dahdahd, Ahmed El Bartali, Nathalie Limodin, Jean-Francois Witz, 2016. In situ 3D characterization of high temperature fatigue damage mechanisms in a cast aluminum alloy using synchrotron X-ray tomography. Scripta Materialia 113, 254–258.

Devaux, J., Gologanu, M., Leblond, J.B., Perrin, G., 1997. On continued voids growth in ductile metals subjected to cyclic loadings. In: Willis, J.R. (Ed.), Symposium on Nonlinear Analysis of Fracture, 299-310.

Eshelby, J. D., 1957. The determination of the elastic field of an ellipsoidal inclusion and related problems. Proc. R. Soc. Lond. A, 241, 376-396.

Hill, R., 1963. Elastic properties of reinforced solids: some theoretical principles. J. Mech. Phys. Solids, 11, 127-140.

Gologanu, M., Leblond, J.B., 1993. Approximate models for ductile metals containing non-spherical voids – Case of axisymmetric prolate ellipsoidal cavities. J. Mech. Phys. Solids, 41(11), 1723–1754.

Gurson, A.L., 1977. Continuum theory of ductile rupture by void nucleation and growth. J. Engng. Mater. Technol. 99, 2–15.

Jan-Hendrik Hommel, J-H, Meschke, G. 2010. A hybrid modeling concept for ultra low cycle fatigue of metallic structures based on micropore damage and unit cell models. International Journal of Fatigue 32 (2010) 1885–1894

Idiart, M., Lahellec, N., 2016. Estimates for the overall linear properties of pointwise heterogeneous solids

with application to elasto-viscoplasticityOriginal Research Article Journal of the Mechanics and Physics of Solids, 97, 317–332

Kailasam, M., Ponte Castañeda, P. (1998). A general constitutive theory for linear and nonlinear particulate media with microstructure evolution. J. Mech. Phys. Solids 46, 427-465.

Kondo, Y., Sakae, C., Kubota, M., Kudou, T., 2003. The effect of material hardness and mean stress on the fatigue limit of steels containing small defects. Fatigue Fract. Eng. Mater. Struct. 26, 675-682.

Lacroix, R., Leblond, J-B., Perrin, G. 2016. Numerical study and theoretical modelling of void growth in porous ductile materials subjected to cyclic loadings. European Journal of Mechanics A/Solids, 55, 100-109.

Lahellec , Pierre Suquet, 2007. On the effective behavior of nonlinear inelastic composites: I. Incremental variational principles. Journal of the Mechanics and Physics of Solids , 55, 9, 1932–1963.

Laws, N., 1973. On the thermostatics of composite materials. J. Mech. Phys. Solids, 21, 9-17.

Leblond, J.B., Perrin, G., Devaux, J., 1995. An improved Gurson-type model for hardenable ductile metals. Eur. J. Mech. A Solids 14, 499–527.

Leblond, J.B., Gologanu, M., 2008. External estimate of the yield surface of an arbitrary ellipsoid containing a confocal void. Comptes Rendus Mécanique, 336(11-12), 813-819.

Lopez-Pamies O., Goudarzi T., Danas K., 2013. The nonlinear elastic response of suspensions of rigid inclusions in rubber: II - A simple explicit approximation for finite-concentration suspensions, J. Mech. Phys. Solids, 61, 19-37.

Limodin, N., Bartali, A. El, Wang, L., Lachambre, J., Charkaluk, E., 2014. Application of X-ray micro-tomography to study the influence of the casting microstructure upon the tensile behaviour of an Al Si alloy. Nucl. Instrum. Phys. Res. Sect. B, Beam Interact. Mater. Atoms 324, 57-62.

K. Madou, J-B. Leblond, L. Morin, 2013. Numerical studies of porous ductile materials containing arbitrary ellipsoidal voids – II: Evolution of the length and orientation of the void axes, European Journal of Mechanics A/Solids 42, 490–507.

Mbiakop,, A., Constantinescu,, A., Danas, K., 2015. On void shape effects of periodic elasto-plastic materials subjected to cyclic loading. European Journal of Mechanics A/Solids, 49, 481-499.

Mbiakop,, A., Constantinescu,, A., Danas, K., 2015. An analytical model for porous single crystals with ellipsoidal voids, Journal of the Mechanics and Physics of Solids, 84, 2015.
void shape effects II: Numerical validation, European Journal of Mechanics A/Solids, 24 ,552-571.

Michel, J.C., Suquet, P., 1992. The constitutive law of nonlinear viscous and porous materials. J. Mech. Phys. Solids 40, 783-815.

Mura, T., 1987. Micromechanics of Defects in Solids, Second, revised edition, Kluwer, Dordrecht.

Papadioti, I., Danas, K., Aravas, N., 2016. A methodology for the estimation of the effective yield function of isotropic composites. International Journal of Solids and Structures, 87, 120-138.

Ponte Castañeda, P., 1991. The effective mechanical properties of nonlinear isotropic composites. J. Mech. Phys. Solids 39, 45-71.

Ponte Casta neda, P., Zaidman, M., 1994. Constitutive models for porous materials with evolving microstructure. J. Mech. Phys. Solids 42, 1459-1497.

Ponte Castañeda, P., 1997. Nonlinear composite materials: Effective constitutive behavior and microstructure evolution. Suquet, P. (Ed.), Continuum micromechanics. In: CISM lectures series. Springer, New York, 61-130.

Ponte Casta neda, P., Suquet, P., 1998. Nonlinear composites. Adv. Appl. Mech. 34, 171-302.

Prager, W., 1949. Recent Developments in the Mathematical Theory of Plasticity. J. Appl. Phys. 20(3), 235-241.

, A. Pirondi, N. Bonora, D. Steglich, W. Brocks, D. Hellmann, 2006. Simulation of failure under cyclic plastic loading by damage models. International Journal of Plasticity 22, 2146–2170.

Rabold, F., Kuna, M., 2005. Cell model simulation of void growth in nodular cast iron under cyclic loading, Computational Materials Science, 32, 489-497

Rice, J. R., 1971. Inelastic constitutive relations for solids: An internal-variable theory and its application to metal plasticity. J. Mech. Phys. Solids, 19(6), 433-455.

Seifert, T., Schmidt, I., 2009. Plastic yielding in cyclically loaded porous materials, International Journal of Plasticity, 25(12), 2435-2453.

Willis, J.R., 1981. Variational and related methods for the overall properties of composites. Adv. Appl. Mech 21, 1-78.